OUTER SPACE AND FOURIER SPACE:

UNDERSTANDING FOREGROUNDS FOR HI EPOCH OF REIONIZATION MEASUREMENTS

Saul Aryeh Kohn

A DISSERTATION

in

Physics and Astronomy

Presented to the Faculties of the University of Pennsylvania

in Partial Fulfillment of the Requirements for the Degree of Doctor of Philosophy

2018

Supervisor of Dissertation — Graduate Group Chairperson

James E. Aguirre
Associate Professor of Physics and Astronomy

Joshua Klein
Professor of Physics and Astronomy

Dissertation Committee:

Cullen Blake, Assistant Professor of Physics and Astronomy

Adam Lidz, Associate Professor of Physics and Astronomy

Elliot Lipeles, Associate Professor of Physics and Astronomy

Masao Sako, Associate Professor of Physics and Astronomy *to my grandparents*

OUTER SPACE AND FOURIER SPACE:

UNDERSTANDING FOREGROUNDS FOR HI EPOCH OF REIONIZATION

MEASUREMENTS

Acknowledgments

Acknowledgements require a certain mindset to be written well.

ABSTRACT

OUTER SPACE AND FOURIER SPACE:

UNDERSTANDING FOREGROUNDS FOR HI EPOCH OF REIONIZATION MEASUREMENTS

Saul A. Kohn

James E. Aguirre

Abstracts are written last.

Contents

List of Tables

List of Figures

Part I

Introduction & Mathematical Formalisms

Chapter 1

The Epoch of Reionization

Chapter 2

Astrophysical Radiation

Chapter 3

Interferometry

Chapter 4

Instruments

In the following chapters I present data and results from a variety of configurations of two massively redundant low frequency interferometers, PAPER and HERA. In this Chapter I describe these instruments (Section 4.1), along with other current and future low frequency interferometers contributing to EoR science (Section 4.2).

4.1 Instruments used in this work

The vision of Hydrogen Epoch of Reionization Arrays was first laid out in the Backer et al. (2010) White Paper. That work proposed three consecutive efforts, improving upon their predecessors, to construct low frequency interferometers capable of detecting the EoR. While the physical feeds and elements of low frequency interferometers were relatively simple to construct, signal processing, calibration and imaging required new hardware and software to be invented. A research community of observational cosmologists interested in cosmological HI had to be nurtured.

The first of the three stages of Reionization Arrays was a parallel effort. The Precision Array for Probing the Epoch of Reionization (PAPER; Section 4.1.1) and the Murchinson Widefield Array (MWA; Section 4.2.2) investigated separate approaches to[1] antenna

[1]Among other things; see Section III B of Backer et al. (2010) for an enumerated list.

design, array layout and calibration techniques, with the objective of setting upper limits on and perhaps detecting the power spectrum of the EoR.

The second stage of the Reionization Arrays brought together the teams from the first stage to design and construct a new interferometer based on the lessons learned from PAPER and the MWA. This new instrument, named *the* Hydrogen Epoch of Reionization Array (HERA; Section 4.1.2) is currently under construction with a build-out schedule that brings new antennas online as they are commissioned. HERA's objective is not only the detection of the EoR power spectrum, but its characterization at very high signal-to-noise. Attempts at low-fidelity imaging of ionized bubbles will be made.

The nature of the third stage is, at the time of writing, somewhat undetermined and contingent on the next decade of funding for low frequency radio astronomy. In the vision of Backer et al. (2010), its objective will be to image structure evolution throughout the EoR.

4.1.1 The Donald C. Backer Precision Array for Probing the Epoch of Reionization (PAPER)

Much of this thesis presents data from PAPER. PAPER was planned, like HERA, as a staged build-out to larger and larger arrays. In each build-out the correlator was replaced, and (nominally) identical antennae and signal chains were added to the existing array. The first iterations of PAPER consisted of 8 dipole antennae in Green Bank, West Virginia and 4 in Western Australia (Parsons et al., 2010). While the Australian site had a far better observing environment in terms of human-generated radio interference, the site in the USA was easier for the team to design and test on. Green Bank was intended as a test site – brighter foregrounds in the Northern Hemisphere and an unprotected low frequency band inhibited the science goals of the experiment. Nonetheless, the array in Green Bank was build-up to 32 antennae and reconfigured from a more traditional "imaging" configuration to a redundant grid, in order to experiment with redundant calibration and increased sensitivity to discrete Fourier modes (Parsons et al., 2012a; Pober et al., 2012). Simultaneously, the PAPER-32 array and correlator were constructed in the Karoo Radio Quiet Zone (KRQZ) in South Africa.

4.1.1.1 The PAPER signal chain

The PAPER signal chain changed little throughout the PAPER build-outs in South Africa, and it remained in operation for the HERA-19 Commissioning Array out to HERA-127. HERA elements are actually PAPER feeds, turned upside-down and suspended over a 14 m dish. This heritage was important to understand when interpreting PAPER or HERA data. We briefly describe the PAPER signal chain below. For a more thorough description, refer to Parsons et al. (2010).

Radio waves were incident upon, and induced a voltage in, a dual-polarization PAPER feed. The feed was a sleeved copper dipole protected by a wire-mesh groundscreen. The sleeve broadened the frequency response of the dipole element, and the groundscreen was used to increase sensitivity to emission from zenith (see Figure 4.1 for a photograph).

Electronics next to the dipole element amplified the voltage by a factor of 10^6, which then propagated down a 150 foot 75 Ω coaxial cable. All cables were of the same length to minimize the amount of extra calibration required per feed, and were above-ground. These cables ran to 8 “receiverators"; RFI-shielded mini-fridges which contained amplifiers which re-amplified the voltage signals by a factor of 10^4 (to correct for signal loss along the 150 ft coaxial cables) and applied an analog bandpass filter. The filter was designed to have a smooth frequency response which was relatively flat between 120 and 180 MHz (e.g. Moore, 2014).

More 50 foot, 75 Ω foot coaxial cables ran from these to an RFI-shielded enclosure for further processing. For PAPER and the HERA-19 commissioning array, this enclosure was a specialized shipping container next to the array. For future HERA build-outs, processing will occur in the Karro Array Processing Building (KAPB) and the receiverator architecture will be replaced with underground “nodes" (see DeBoer et al. (2017) for more detail).

Figure 4.1: An image of a PAPER dipole element with its groundscreen.

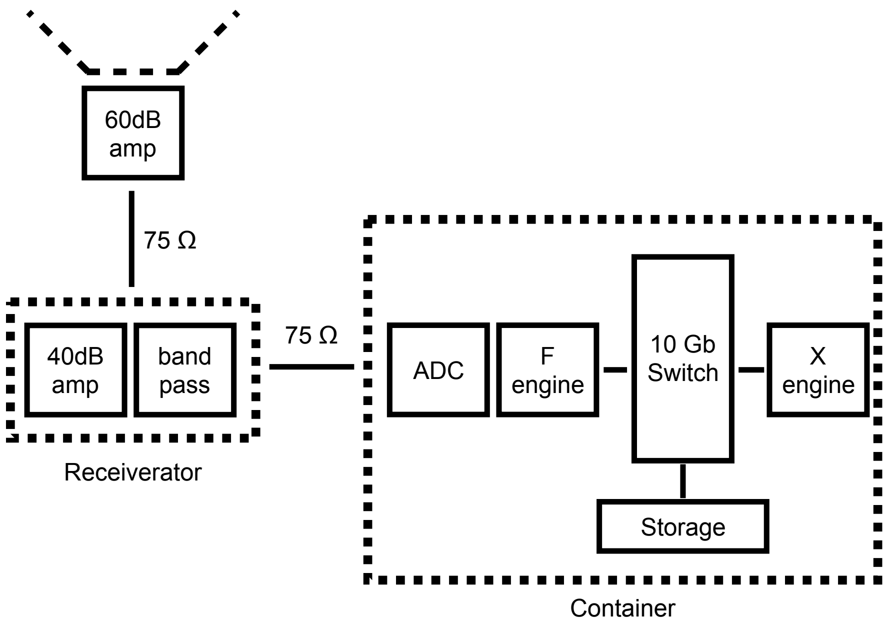

Figure 4.2: A diagram of the PAPER-128 signal chain. Square-dotted lines indicate RFI-shielding.

The filtered analog signal was then digitized with a sampling rate of 100 MHz and passed through an F-engine which Fourier transforms the signal using a 4-tap polyphase filter bank (which allowed for a smooth frequency and Fourier-space response; Price (2016)). The integration time of each Fourier transform was 10 s. The Fourier transformed signals were distributed over a 10 Gigabit Ethernet switch to the X-engine (Parsons et al., 2008), which cross-multiplied all signals with each other to form visibilities, storing them in MIRIAD files.

A summary of the system described above is shown in Figure 4.2.

4.1.1.2 PAPER-32

The PAPER-32 array in South Africa used a highly redundant configuration in order to take the measurements resulting in, at the time, the strongest upper limits on the EoR

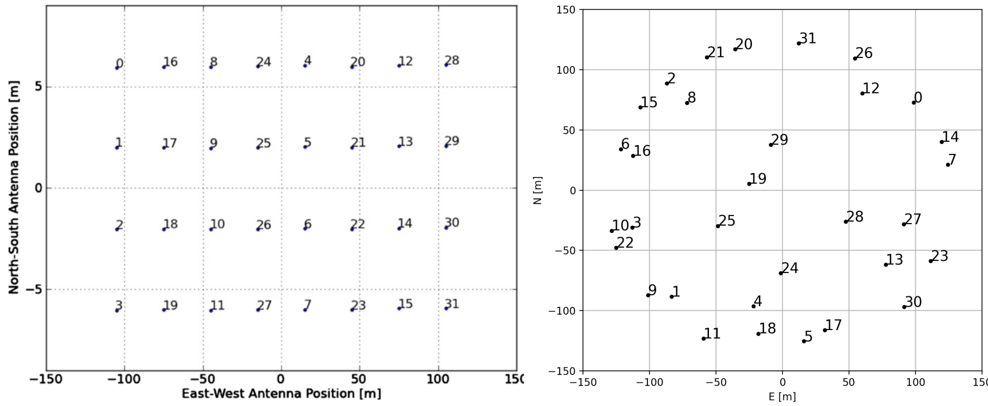

Figure 4.3: The array layouts of the PAPER-32 element deployment in South Africa. *Left*: The redundant grid. Four rows, with each element 30 m from the next in the East-West direction, and closely-packed ($\sim$4 m) in the North-South direction. Figure taken from Parsons et al. (2014). *Right*: The polarized imaging array. Elements were arranged in a pseudo-random scatter.

power spectrum (Parsons et al., 2014; Jacobs et al., 2015; Moore et al., 2017, sections of Moore et al. 2017 are presented in Chapter 8). The array was in redundant configuration from December 2011 to February 2012. For three nights in September 2011, the 32 elements were reconfigured into an polarized imaging configuration. The results from this deployment were used to make the first 2D power spectra of polarization, presented in Kohn et al. (2016) and in Chapter 9. For images and a brief description, see Figure 4.3.

4.1.1.3 PAPER-64

During the PAPER-32 EoR integration, there were actually 64 antennas present in the Karoo, South Africa. However, the correlator at that time could only process 64 voltage streams – enough for 32 dual-polarization antennae. This is why 64 element single-instrument-polarization imaging results were published prior to any PAPER-32 studies (Jacobs et al., 2013; Stefan et al., 2013). EoR integrations in the 64 element redundant

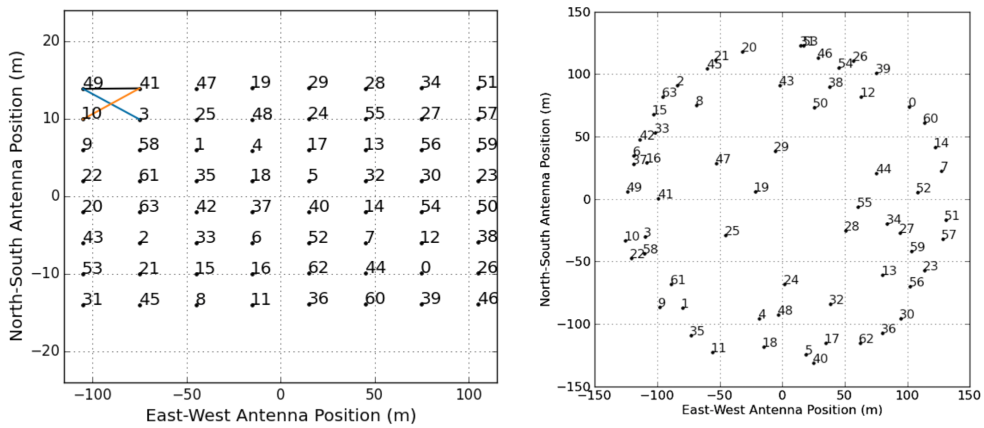

Figure 4.4: The array layouts of the PAPER-64 deployment. *Left*: The redundant grid, built-out from the PAPER-32 grid. Figure taken from Ali et al. (2015), which highlights the baseline-types used for power spectrum measurements. *Right*: the imaging array, used by Jacobs et al. (2013) to set an absolute flux scale for PAPER experiments. Figure taken from Jacobs et al. (2013).

configuration were only possible after a new correlator was produced in 2012. Results from this array were published in (Ali et al., 2015; Pober et al., 2015, Cheng et al. *in prep.*, Kolopanis et al. *in prep.*). Diagnostic results from the PAPER-64 redundant configuration that informed studies of time-averaged visibilities are presented in Chapter 12. The array layouts are shown in Figure 4.4.

4.1.1.4 PAPER-128

The culmination of the PAPER experiment was the 128 element deployment. There were two observing seasons recorded: November 2013 to March 2014, and July 2014 to January 2015. In this configuration, 112 antennas were laid-out in a redundant grid with 15 m East-West spacings and 4 m North-South spacings. The remaining 16 antennas were arranged in 'out-rigger' and 'in-rigger' positions to increase *uv*-coverage and enable some

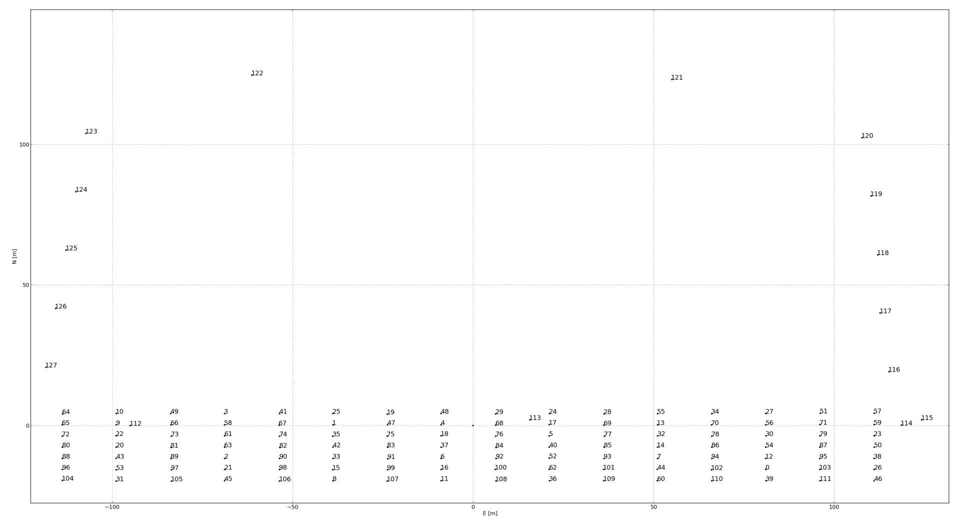

Figure 4.5: The PAPER-128 array layout. 112 antennas were laid-out in a redundant grid with 15 m East-West spacings and 4 m North-South spacings, and the remaining 16 antennas were arranged in 'out-rigger' and 'in-rigger' positions to increase *uv*-coverage.

level of imaging. Results from the first observing season of this array are presented in Chapters 6, 7 and 11. The array layout is shown in Figure

4.1.2 The Hydrogen Epoch of Reionization Array (HERA)

HERA was ranked as the "top priority in the Radio, Millimeter, and Sub-millimeter category of recommended new facilities for mid-scale funding" by the National Research Council Decadal Survey in astronomy and astrophysics (NRC, 2010). It brought together the largely US-based experts working on PAPER and the MWA to construct a new low-frequency array on the PAPER site in South Africa. The array, comprised of 14 m diameter dishes, was designed to be build-out in stages of close-packed hexagons of increasing size. For a full description of the instrument, refer to DeBoer et al. (2017).

The design of the HERA dish, feed, antenna layout and signal chain are intimately related to lessons learned by the PAPER and MWA EoR teams about the nature of EoR measurements (e.g. Thyagarajan et al., 2015b). One of the major considerations was

Figure 4.6: *Left*: a rendering of the 320 element HERA core. *Right*: the 19 element commissioning array (with the construction team). Leftover PAPER dipoles can also be seen in the background, forming three experimental arrays (described in Section 4.1.2.1). Figure taken from DeBoer et al. (2017)

how the instrument couples to the bright foregrounds, and how to control that coupling – the paradigm of the “wedge" and the “EoR Window", which are discussed in detail in Chapter 5. Measurements based on prototype feeds were presented in (Ewall-Wice et al., 2016; Neben et al., 2016, Patra et al. *submitted*).

HERA is a staged experiment, building-out in close-packed hexagons from a 19 element commissioning array, to 37, 127, 240 and finally 350 elements (320 in a dense, fractured core and 30 out-riggers, see (Dillon & Parsons, 2016) for more detail). Figure 4.6 shows a rendering of the core alongside an image of the HERA-19 commissioning array.

4.1.2.1 HERA-19 Commissioning Array

In October 2015 a HERA commissioning array was completed, connected to the PAPER-128 256-input correlator. This array comprised of four separate components: the first 19 HERA dishes in a close-packed hexagon (HERA-19), 19 PAPER dipoles at the central locations of a hexagon of future HERA dishes (the “PAPER-Hex"), 40 PAPER dipoles in a redundant grid where every-other dipole was rotated 45° (to experiment with different polarization bases; “PAPER Pol"), and the remaining inputs filled with PAPER dipoles arranged in a pseudo-random scatter for imaging (“PAPER-Img"). Studies with this array are presented in Chapter 6 and 10. A diagram of the commissioning setup is shown in

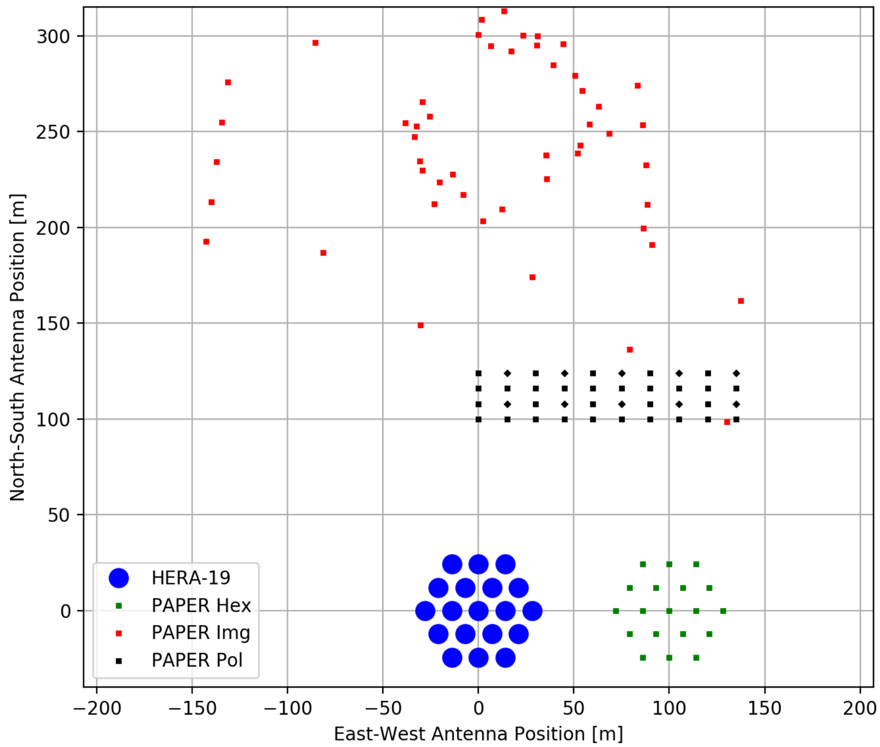

Figure 4.7: Positions of antennae in the HERA-19 Commissioning Array (including the experimental “subarrays").

Figure 4.7.

4.1.2.2 Future HERA Build-Outs

Each HERA element is much more sensitive than a PAPER element, based purely on collecting area. Figure 4.8 illustrates the varying sensitivities and collecting areas of different arrays and their elements, respectively. PAPER-128 was forecast to make marginal detections of the EoR power spectrum after $\sim$1000 hours of integration – HERA-127 should be capable of characterizing the EoR power spectrum at high significance, and the full HERA-350 array will be an extremely powerful survey instrument (e.g. Pober, 2015).

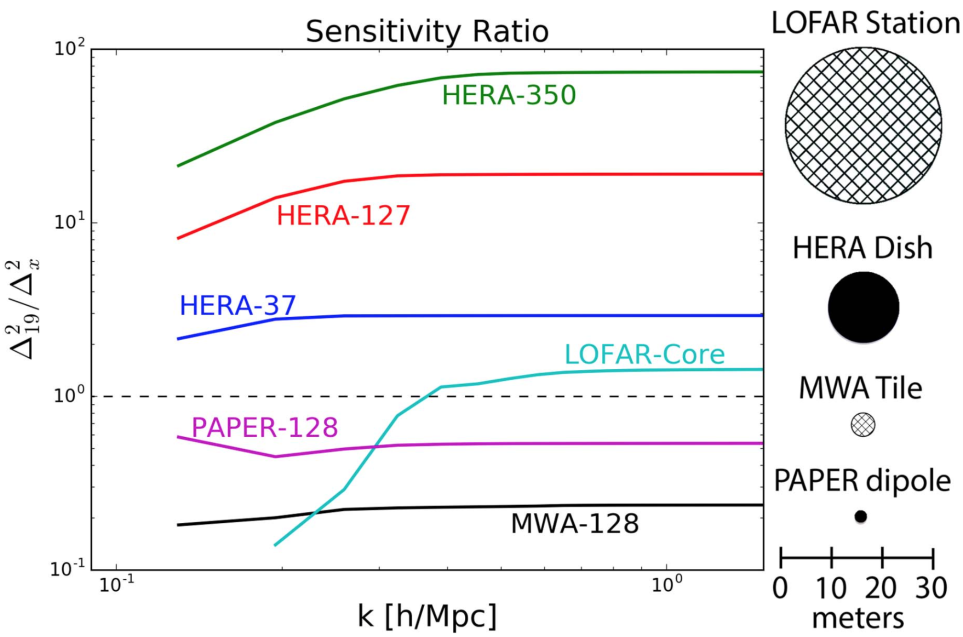

Figure 4.8: Instantaneous array Sensitivities as a function of *k*-mode (e.g. Chapter 5) relative to HERA-19. Differing element collecting areas are shown on the right. Taken from DeBoer et al. (2017).

We present forecasts for this future instrument in Chapter 13.

4.2 Other current and future interferometers

PAPER and HERA were not the only instruments researching the EoR and how to detect it. Several low-frequency interferometers around the world are contributing to the understanding of the EoR and the difficulties of observing it. Below I briefly describe a few of the leaders of the field – but it is not an exhaustive list.

4.2.1 The Low Frequency Array (LOFAR)

The LOw Frequency ARray (LOFAR) is an interferometer made-up of “stations", the core of which are arranged in a random scatter near Exloo in the Netherlands (van Haarlem et al., 2013). LOFAR baselines extend across Europe with stations in Ireland, Sweden, Germany, Poland and other locations. These extremely long baselines can provide LOFAR with exquisite imaging capabilities.

LOFAR has detected diffuse, linear polarization structures that may be related to the Milky Way's magnetic field and interstellar medium (Jelić et al., 2015). Patil et al. (2017) presented deep limits on the EoR power spectrum from one night of LOFAR data (also see Yatawatta et al. (2013)). A series of publications has investigated polarization in Fourier space (Jelić et al., 2014; Asad et al., 2015, 2016, 2017) – results that we build upon and verify throughout this work.

4.2.2 The Murchinson Widefield Array (MWA)

The Murchinson Widefield Array (MWA), based in Murchison Radio-astronomy Observatory in Western Australia, is composed of 256 “tiles" of 16 feeds each. At the time of writing, 72 tiles are arranged in compact hexagonal configurations in an effort to increase EoR sensitivity while retaining imaging capabilities with the rest of the array. The most complete low-frequency catalog of the southern sky, GLEAM, was presented by Hurley-Walker et al. (2017).

The MWA uses separate analysis pipelines for its EoR measurements (Sullivan et al., 2012a; Jacobs et al., 2016; Trott et al., 2016), an concept that will be implemented on future HERA measurements. The MWA has detected polarized signal from diffuse Galactic emission (Lenc et al., 2016, 2017) and set deep limits on the EoR power spectrum (e.g. Dillon et al., 2014, 2015). Pioneering work on the ionosphere was accomplished using MWA data (e.g. Loi et al., 2015), which we discuss in Chapter 8.

4.2.3 Square Kilometer Array – Low band (SKA-Low)

The Square Kilometer Array (SKA) will be built on two sites: the Karoo Radio Quiet Zone, currently occupied by HERA, will be the central location of the “high–mid band"

(350 MHz – 14 GHz; “SKA-Mid") observatory and the Murchinson Radio-astronomy Observatory, currently occupied by the MWA, will be the central location of the “low band" observatory (50 – 350 MHz; “SKA-Low").

SKA-Low will consist of over 100,000 receiving elements in an imaging configuration. It will be the most powerful low-frequency radio telescope ever created, and be used not only for EoR science but a host of low-frequency science objectives (e.g. Carilli & Rawlings, 2004; Schilizzi et al., 2007; Dewdney et al., 2009). Learning from the work of EoR teams working on PAPER, HERA, MWA, LOFAR and other instruments will be crucial to the success of SKA-Low’s EoR science goals.

Part II

Structure in Fourier space

Chapter 5

Peering through the EoR Window

Chapter 6

Data Preparation and Processing

The data volume of interferometric measurements inherently scale as the square of the number of antennas in the array (N_{ant}). Not only does the sheer volume of data from large-N_{ant} arrays pose a problem for data storage, but also it requires precise and efficient efforts to quality assure (QA) the data.

In this chapter, I will outline some of the efforts involved in data preparation, preprocessing and QA that are required for an EoR power spectrum estimate.

6.1 Data Compression

The PAPER-128 correlator produced 288 MIRIAD files per night. Each of these contained 8126 baselines, and each baseline contained visibilities over 1024 98 kHz frequency channels and 56 10 s time integrations. The four instrumental polarizations were in separate files. In sum, each file was 4.2 GB which meant that each night 1.2 TB of data were recorded.

In order to efficiently transport the data over Gigabit Ethernet from the Karoo Radio Quiet Zone (KRQZ) to Cape Town, and from Cape Town under transatlantic cables to Philadelphia, some compression was required. It was also required that such a compression, while lossy, did not effect the targeted cosmological signal.

6.1.1 Delay–Delay-Rate Filtering

The compression algorithm implemented for PAPER observations, Delay–Delay-Rate (DDR) filtering, was introduced in Parsons & Backer (2009) described in Parsons et al. (2014), and we briefly review it below.

The geometric delay of a celestial signal, originating form direction $\hat{s}$, incident on an interferometric baseline described by vector $\vec{b}$, is

$$\tau_g = |\vec{b} \cdot \hat{s}|/c \tag{6.1}$$

where c is the speed of light. This relationship implies that τ_g is bounded for a given baseline

$$-|\vec{b}|/c \leqslant \tau_g \leqslant |\vec{b}|/c \tag{6.2}$$

Equation 6.2 therefore gives the maximum value of $|\tau_g|$ physically meaningful for a given array – the maximum baseline length in that array, divided by c. For PAPER, the maximum baseline length is 300 m, corresponding to $\max(|\tau_g|) = 1\mu$s. As reviewed in Chapter 5, the delay axis may be accessed by Fourier transforming a visibility along the frequency axis. Once in delay space, power at delays larger in magnitude than 1μs could be removed. With a sufficiently large frequency bandwidth, this would not produce aliased signal, according to the critical Nyquist rate. By using the 1μs as a delay bound for all visibilities, the frequency axes of all compressed visibilities remained the same (reduced in number from 1024 to 203), which while sub-optimal from a compression point of view, allowed for ease of programming at later stages.

A similar geometric bound can be obtained by Fourier transforming the time axis of visibilities, provided that they were obtained in drift-scan mode (see Chapter 3). Parsons & Backer (2009) showed that the rate at which the geometric delay on an interferometric baseline changes is governed only by the position of the array on Earth, and the Earth's rotation:

$$\dot{\tau}_g = -\frac{\omega_\oplus \cos\delta}{c}\left(b_x \sin\alpha + b_y \cos\alpha\right) \tag{6.3}$$

where $\omega_\oplus$ is the angular frequency of the Earth's rotation, α and δ are the hour-angle and declination of a point on the celestial sphere, respectively, and $\vec{b} = (b_x, b_y, b_z)$ is the baseline vector expressed in equatorial coordinates.

For arrays not close to the geographic poles, $|b_y| \gg |b_x|$, there is a maximum rate of change (corresponding to (α, δ) = (0, 0)), producing a bound on $\dot{\tau}_g$:

$$-\omega_\oplus |b_y|/c \leqslant \dot{\tau}_g \leqslant \omega_\oplus |b_y|/c \tag{6.4}$$

for a 300 m East-West baseline, the maximum delay-rate is approximately $\max(|\dot{\tau}_g|) = 0.07\,\mathrm{ns\,s^{-1}}$. This delay-rate was not Nyquist sampled by a single PAPER file: requiring the previous and next files generated for that polarization to be appended on either side of each visibility's time axis to prevent aliasing from the decimation. For the large scale processing of months of data, this required a software pipeline described in Section 6.1.2.

There are also other issues with DDR compression, largely associated with instrument systematics. Delay transforms rely on the fact that the bright foregrounds that dominate the measured signal are spectrally smooth, and that the frequency response of the instrument is also spectrally smooth: this of course is the basis for the EoR window paradigm reviewed in Chapter 5. Likewise, delay-rate filtering assumes temporal smoothness. Radio Frequency Interference (RFI) signals created by human communications violate both models of smoothness, since they are typically confined to narrow bandwidths (creating sharp spikes along the frequency axis) and may be transient (creating sharp spikes along the time axis). This requires steadfast identification and flagging algorithms for RFI (see Section 6.2), and some variety of interpolation, fitting, or CLEANing across the flagged regions prior to compression.

By DDR filtering of PAPER-128 data using a 300 m baseline to set the width of the filters we were able to reduce the volume of the data by an approximate factor of 70.

6.1.2 Software Implementation

The first season of PAPER-128 data, due to a variety of circumstances, required compression on the computing cluster at the University of Pennsylvania. The raw data were stored on a high-volume drive that was able to connect with the cluster via a low-speed switch. The hardware capable of performing any sort of high-performance processing (i.e. holding the data in RAM) were ten “compute nodes" connected to the cluster via a high-speed switch, and mounted in an NFS architecture. The compute nodes could only hold $\sim$ 10 PAPER-128 files in storage.

The processing stages for compression of a night of PAPER data, described below, required knowledge of the location and compression state of not only individual files, but also the neighbors-in-time of the file in question, in order to implement the DDR filter described above. To supervise the compression we created a MySQL database, which we interacted with via Shell and Python scripts. The database contained a table for the data files under processing and their compression state, a table of neighbor-relations, a table of file details, and a table of the processing nodes available. The schema of this database is shown in Figure 6.1.

To implement the compression, per file, the following steps were required:

1. Copying the file from the storage volume to the cluster. For a single night of data, this required roughly 8 hours.

2. Copying the file from the cluster to the compute node. This required roughly 5 minutes.

3. Generate copy of the file, with metadata corrections. This required roughly 1 minute.

4. Delete the raw file.

5. RFI-flag the high frequency-resolution data. This required roughly 2 minutes.

6. Delete the metadata-corrected file.

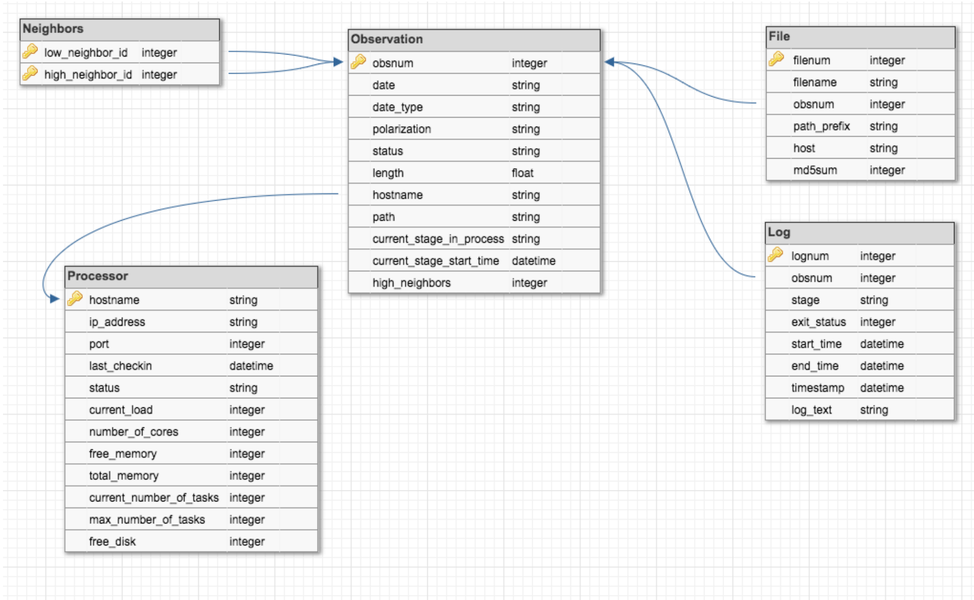

Figure 6.1: The schema of the database used to organize and implement PAPER data compression.

7. Acquire time-neighbors to the file in question, and bring them to the RFI-flagged stage. The time required for this stage varied with cluster activity, but usually required roughly 20 minutes.

8. DDR filter the RFI-flagged data, using an high-tolerance iterative CLEAN. This required roughly 20 minutes.

9. RFI flag the compressed data (coarse flagging), saving the flags to a separate file. This required roughly 1 minute.

10. Apply the coarse RFI flags to the *uncompressed*, RFI-flagged data. This required roughly one minute.

11. DDR filter the now twice-RFI-flagged data, using a low-tolerance iterative CLEAN. This required roughly 120 minutes.

12. Copy compressed data to the cluster.

13. Delete the twice-RFI-flagged data.

14. If the once-RFI-flagged data are not required as neighbors, delete them.

15. Delete the compressed data from the compute node.

16. If neighbors have already been compressed, delete them, otherwise begin their compression.

17. After all files are compressed, delete the uncompressed files from the cluster.

In total, this meant that across ten compute nodes, and efficient use of the fact that the neighbors could progress through the processing stages while the central file was being compressed, meant that it took roughly 20 to 24 hours to compress a night of observations.

6.2 Radio Frequency Interference

As noted above, RFI was able to introduce spectral and temporal structure that would cause ringing in the data during compression if it was not flagged. This meant that both identification and characterization of RFI was crucial to the scientific goals of the PAPER and HERA experiments. In Section 6.2.1, I present characterization of RFI in the second season of PAPER-128 data. By averaging flags in local time I was able to investigate "repeat offender" frequency bands and identify outlying "quiet" and "loud" days. In Section 6.2.2 I analyze RFI flags from the first Internal Data Release (IDR1) of HERA commissioning data, which contained 19 HERA feeds suspended above 5 m dishes in a close-packed hexagon, and 19 PAPER feeds in the same positions as the central dishes, allowing us to investigate the difference in flagging between feeds at different altitudes.

6.2.1 PAPER-128

The PAPER-128 2014 observation season ran from 18th June 2014 through the 30th April 2015. During this run, some 150 nights of data were recorded. A "night", which I will refer to using the JD at the start of observations, consists of twelve hours of observation from 6pm to 6am South African Standard Time (SAST). Observations as processed by the PAPER correlator are recorded in MIRIAD uv files. These files contain visibilities for each antenna pair in the array. Each integration is 20 seconds long over 1024 frequency bins from 100 to 200 MHz. Each uv file contains 56 integrations per antenna pair, and 72 uv files are recorded per linear polarization (xx, xy, yx, yy) per night.

Early in the PAPER data compression process, visibilities are flagged for RFI. This is accomplished by the aipy script *xrfi_simple.py*, which takes the derivative of the frequency axis of all baselines associated with a single antenna, and flags any frequencies with a derivative $\geqslant 6\sigma$ above the mean. We always flag the band-edges ($\sim$7 MHz on each side), since these frequencies are not useful to us, and always flag the 137$\pm$0.6 MHz band associated with ORBCOMM satellite network transmissions. This process is repeated per integration within each uv file and stored in a Python numpy zip (npz) file. This means that any baseline associated with antenna 1 can contribute a flag to the resultant npz file, which in turn is applied to the data.

The result is 280 files of high-time and -frequency resolution files per night per linear polarization containing information about the RFI environment of the HERA site. I report on the properties of these flags in time- and frequency-space over the 2014 observation season. This section is organized it as follows: in Section 6.2.1.1, I analyse the average properties of RFI over the season by stacking flags in local time and normalizing appropriately. In Section 6.2.1.2 I address nights with particularly strange RFI properties. I discuss the implications of my findings in Section 6.2.1.3.

6.2.1.1 Average Properties

In order to assess the average properties of the RFI environment, I calculated a weighted average of flags over the season. Over 150 nights, one-time occurrences are washed-out beneath the 1% level, allowing me to assess persistent issues.

Nominally, each night should grant 3920 integrations-worth of flags over 1024 frequency bins, per linear polarization. In reality, most of the time this holds true, but occasionally not all files are compressible (hence failing to generate flags) or observations fail to start at the correct time (so there are no data to flag). Also, in the event of an X-engine failure within the correlator, contiguous chunks of the band (in eighths, i.e. 25 MHz across) are flagged-out, usually for the rest of the night.

For this reason, I calculated a weighted average of the flags across the season, but neglected nights with correlator failures or late starts. Weights were simply the number of nights that contained that integration-bin in SAST. The resultant “flag density waterfall" is shown in Figure 6.2. The color scale is indicative of flagging frequency across the season, and line plots above and to the right of the the waterfall showing the percentage of times and frequencies that were flagged, respectively.

A summary of the persistent (flagged $\geq 1\%$ of the time per channel) RFI frequencies can be found in Table 6.2.1.1. I have investigated each frequency and tried to find the most likely source for each. In most cases, this required looking at the properties in time as well as frequency. Others were more obvious from frequency alone, e.g. the 149.8 MHz transmission frequency from the International Space Station (ISS). Still others I could not track down a convincing explanation for, and these are listed with a ‘?’. A ‘?’ next to a possible cause indicates that the listed cause is the most prevalent at that frequency, but that the temporal properties of that cause do not necessarily make sense. Many of the characterizations arise from the South African Table of Frequency Allocations (SATFA; Staatskoerant (2008)).

Figure 6.3 shows the detail of the top panel of Figure 6.2. This figure highlights the broad swath of the band from roughly 150 to 180 MHz that was, on average, clear of RFI. This roughly corresponds to 21 cm redshifts $z = 6.9$ to 8.5. This is one of the reasons that the Parsons et al. (2014) and Ali et al. (2015) limits on the 21 cm power spectrum concentrated on this redshift range – there were simply more unflagged data to average-down with. Furlanetto et al. (2006) show that the $z \sim 8$ universe can be considered roughly coeval over an $\sim$8 MHz bandwidth. As such, the 30 MHz chunk could be used to

Table 6.1. PAPER-128 RFI frequencies and brief characterization for the averaged flags.

ν MHz	Flagged %	Cause (Possible)	Notes or Time (SAST) Characterization
103 ± 3	100	BAND EDGE	Built-in to flagger.
107.25 ± 0.25	2.6	FM radio	Constant background at 2% level
107.55 ± 0.05	1.9	FM radio	Constant background at 2% level
108.1 ± 0.4	9	FM radio?	Rises with time, peaking at midnight and 4am
109 ± 0.4	11.5	FM radio?	Rises with time, peaking around 4am
112.8 ± 0.1	1.4	Aircraft?	Constant background at 1% level
114.05 ± 0.85	3.7	?1	Decreases till midnight; peak at 4am
116.55 ± 0.35	2.2	?2	Peak at midnight
120.15 ± 0.35	3.2	Aircraft	Roughly follows CPT$\leftrightarrow$JNB flight times
124.95 ± 0.35	5.5	Aircraft	Roughly follows CPT$\leftrightarrow$JNB flight times
130.25 ± 0.55	4.3	?3	Falls (7pm) and rises (3am) steeply
131.75 ± 0.35	10.3	Aircraft?	Peaks at 6:30, 7:30, 8:30, 9:30, 10 and then a steep falloff
136.05 ± 0.45	33.1	Radar?	Decreases over night
137.35 ± 0.85	100	ORBCOMM	
141.45 ± 0.35	2.1	Mobile phones?	High until 9pm, then at background 1% level
145.85 ± 0.45	10.7	Amateur radio	Strong 9pm-1am – this is the official downlink for ISS-HAM
149.75 ± 0.55	90.7	ISS	"Beeps", but in stacked data peaks 2am
175.15 ± 0.35	20.5	VHF TV (video)	Channel 4. Peaks at 8:30pm, then falls to background 7%
181.15 ± 0.15	1.6	VHF TV (audio)	Channel 4. 2% level turns-off at 10pm
182.15 ± 0.35	75	?4	Decreases until 10pm (to 15%), when it begins a slow rise again
183.2 ± 0.5	89.7	VHF TV (video)	Channel 5. Rises throughout night.
186.25 ± 0.35	4.6	?5	Extreme turn-off at 9:45
189.15 ± 0.35	41.4	VHF TV (audio)	Channel 5. Rises throughout night.
189.9 ± 0.4	100	VHF TV	Channel 6. Built-in to flagger.
191.1 ± 0.3	100	VHF TV	Channel 7. Built-in to flagger.
196 ± 4	100	BAND EDGE	

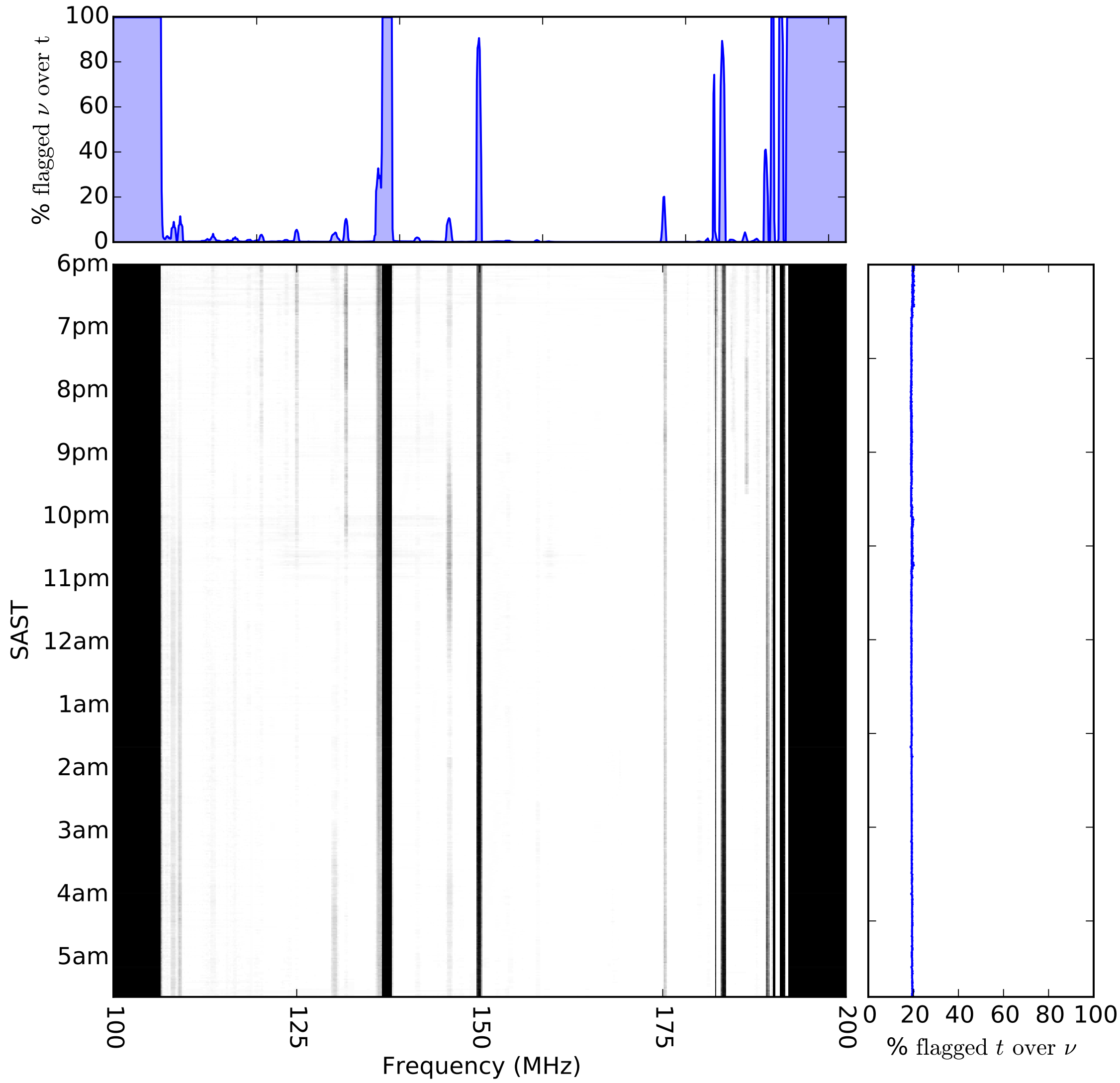

Figure 6.2: A waterfall plot of RFI flags averaged over 150 days of data. The gridding process is described in the text. Above the waterfall I show the percentage of the season each frequency is flagged, and to the right I show the percentage of frequencies that are flagged per integration.

create ∼3 power spectra, as demonstrated in Jacobs et al. (2015). As we show below, the deactivation of VHF TV broadcasts could enable measurements up to the band edge.

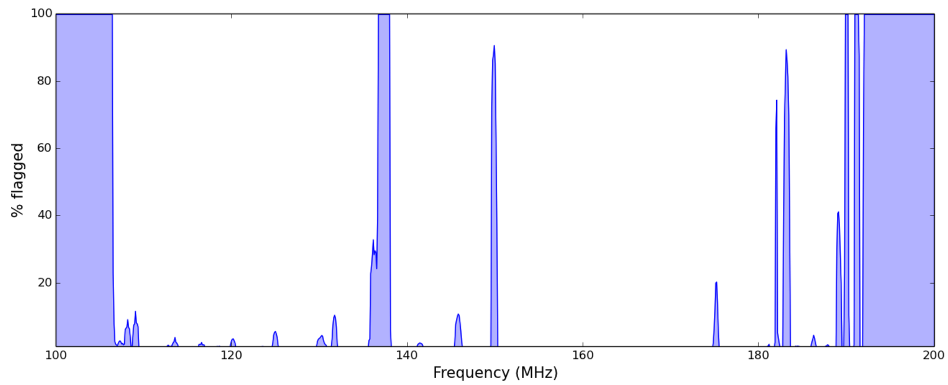

Figure 6.3: The percentage of time that each frequency was flagged over the season.

FM Radio

SATFA lists the frequency band 87.5–108 MHz as available for FM radio broadcasts, leading me to postulate that the low-level RFI we observed in the 107.25 $\pm$ 0.25 and 107.55 $\pm$ 0.05 MHz bands had FM radio as the leading cause. The 108.1 $\pm$ 0.4 and 109 $\pm$ 0.4 MHz bands were outside of the official range, and exhibit odd temporal properties for human activity – two peaks at midnight and 4am – with a increasing number of flags throughout the average night (see Figure 6.4).

Aircraft communications

It was difficult to argue that the 112.1$\pm$0.1 MHz signal is caused by aircraft communications since it maintained a constant background level. However, SATFA listed this frequency as reserved for aircraft communications and it has been used in the past as a calibration frequency for aircraft instruments South African Civil Aviation Authority (2008).

The other aircraft frequencies were obvious, because they closely traced the 2-hour

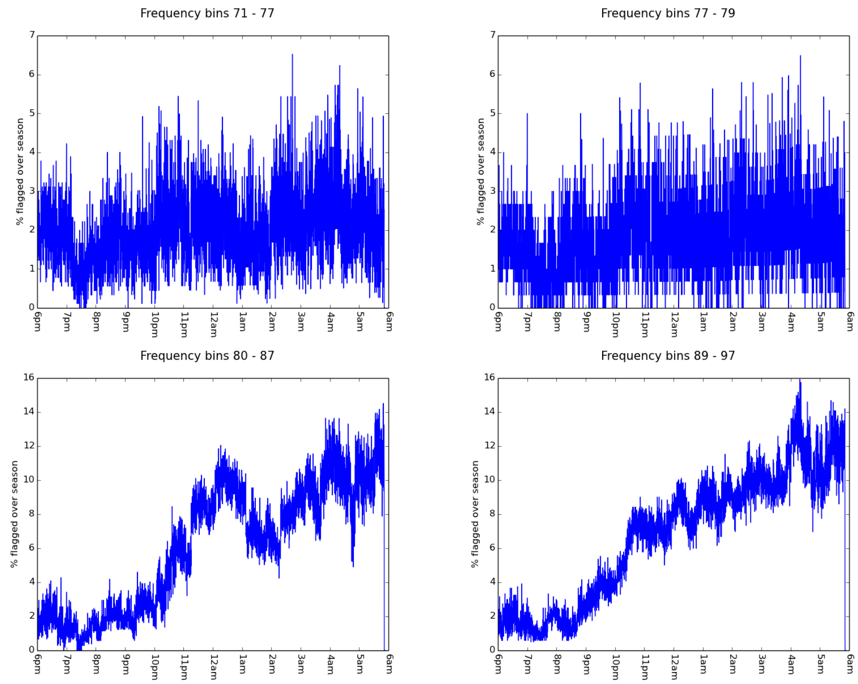

Figure 6.4: Possible FM radio contamination in the *Top, left to right*: 107.25±0.25 and 107.55±0.05 MHz bands, and *Bottom, left to right*: 108.1±0.4 and 109±0.4 MHz bands.

flight from Cape Town to Johannesburg[1]. An example (120.15±0.35 MHz) is shown in Figure 6.5. SATFA reserved frequencies 108–117.975 MHz for aeronautical radionavigation and 117.975–137 MHz for aeronautical mobile. In Table 6.2.1.1 I listed 131.75±0.35 MHz as caused by aircraft since it falls in the aeronautical mobile band, but it does not follow the flight patterns as closely as the other bands.

Orbital communications

ORBCOMM Inc.'s constellation of 29 LEO communication satellites is a well-known contaminant of the low-frequency sky, dominating over any astronomical signal at 137–138 MHz (although each satellite emits within a 20 kHz band). For this reason there was

[1] Credit to Danny Jacobs for first spotting this and noting it in an internal PAPER circular in December 2009.

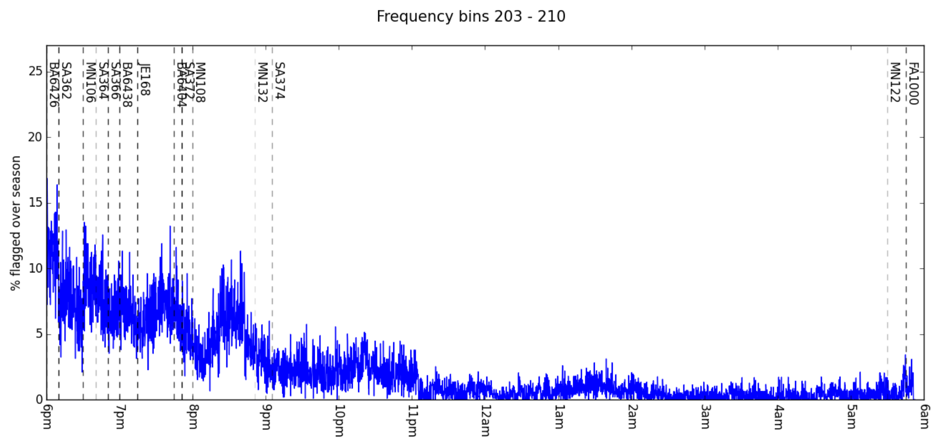

Figure 6.5: Flights from Cape Town to Johannesburg correspond to RFI in the 120.15±0.35 MHz channels. Vertical dashed lines indicate a flight leaving Cape Town (flights from Johannesburg are roughly concurrent) and the flight code is listed. The transparency of a line is inversely proportional to how many days a week that flight is scheduled for. The flight is 2 to 2.5 hours long – and about 2 hours after the last flight of the day, the flags fall to background level (but notably, not always to zero).

built-in flagging at 137.35±0.85 MHz within the compression pipeline.

The largest contaminant without built-in flags in the pipeline were communications from the ISS. The 149.75±0.55 MHz transmissions were semi-regular in time; they ‘beep’.

Onboard the ISS are HAM radio devices. Some countries have also launched satellites with these onboard, one of the purposes of which is to provide HAM radio operators something in space to communicate with. These devices are licensed to operate at 145.2 and 145.8 MHz, and SATFA listed the 144-146 MHz band as reserved for ‘Amateur–Satellite’ communications. We detected RFI at 145.85±0.45 MHz, although strong signal across ∼10% of the season that occurs 9pm-1am argues against human operation.

Mobile phones and VHF TV

A weak RFI signal at 141.45±0.35 MHz was within the ‘mobile 1 BTX’ and aeronautical mobile band in SATFA, but other than this single listing I did not build a strong case for the signal's cause.

VHF TV is broadcast over specifically-spaced video and audio frequencies. The strong signals at 183.2±0.5 MHz and 189.15±0.35 MHz had almost identical gradients for the percentage of flagging as a function of time of night. These frequencies corresponded exactly to Channel 5 of South African System I 625-line VHF TV signals for video and audio transmission, respectively. Similarly, the weaker signals at 175.15±0.35 and 181.15±0.15 MHz corresponded to Channel 4's video and audio transmission, respectively, but they did not share the same temporal properties.

Unidentified sources

There were 5 RFI frequencies in the averaged data that I could not identify the sources of: weak emissions (flagged $< 5\%$ of the season) at 114.05±0.85, 116.55±0.35, 130.25±0.55 and 186.25±0.35 MHz, and one strong emission at 182.15±0.35 MHz. The variation of each source with time is shown in Figure 6.6. The 186.25±0.35 MHz had a sharp turn-off around 9:45pm each night, suggesting that it originated from some kind of automated device.

6.2.1.2 Individual Properties

Using the flags per night, I was able to assess the total number of flags as a percentage of the waterfall (i.e. $N_{\mathrm{flags}}/(3920 \times 1024)$). The average flagging per night was 19.2±0.5%, which was dominated by the permanent flagging of ORBCOMM and band edges. Four nights deviated from the average by a $\geq 2\sigma$ excess: JDs 2456965, 2456732, 2456958 and 2457038. Their flag waterfalls are shown in Figure 6.7 (2456732, 2456958 and 2457038) and Figure 6.8 (2456965). While the strange nature of night 2456965 is discussed below, the three others followed the pattern of having strong contamination from FM and aircraft communication bands, but also had broadband 'pulses' up to about 20 minutes in length. The source of these broadband pulses is not well understood, although it was clear that

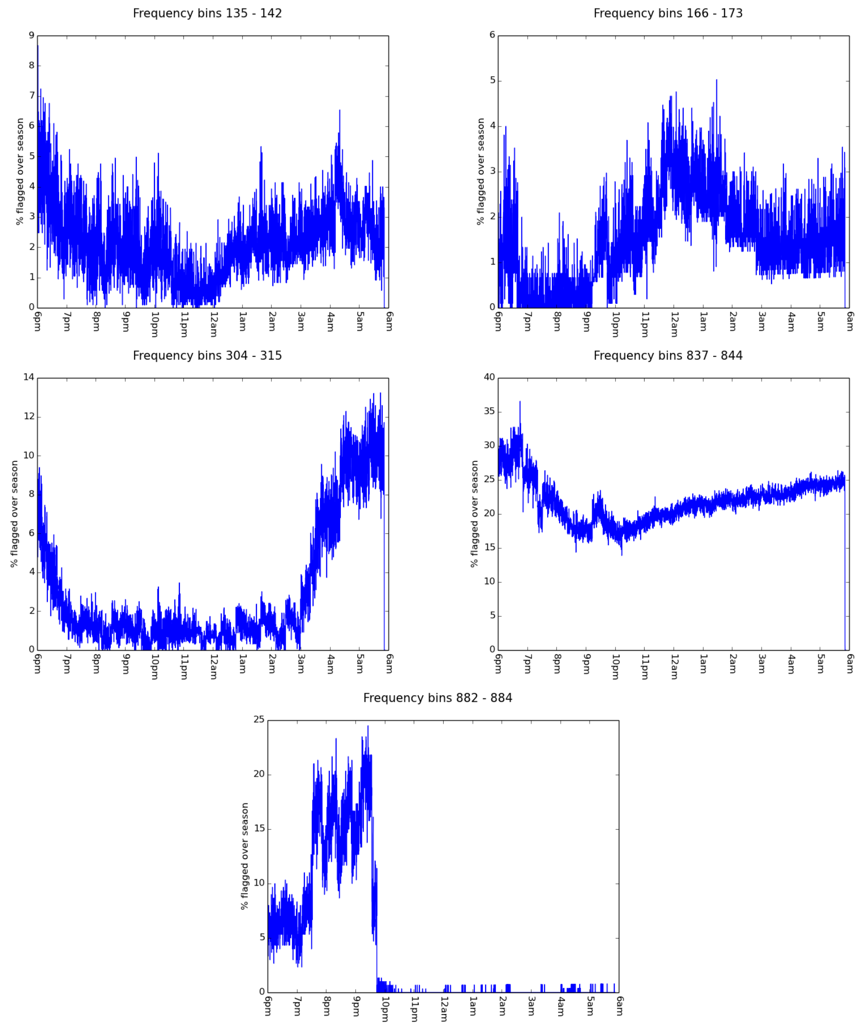

Figure 6.6: The temporal profile of the 5 RFI frequencies with unidentified causes. *Top, left to right:* 114.05±0.85 and 116.55±0.35 MHz. *Middle, left to right:* 130.25±0.55 and 182.15±0.35 MHz. *Bottom:* 186.25±0.35 MHz. The 182.15±0.35 MHz frequency is flagged a large amount of the time, making it our most-offending unidentified source.

ORBCOMM tends to spill outside of its allocated band on occasion.

JD 2456965 was easily the worst offender, and it exhibited a strange signal that wanders in frequency and time close to the ISS band. An event of note on this date (23rd November 2014) was a Soyuz FG launch that docked with the ISS – this may have been

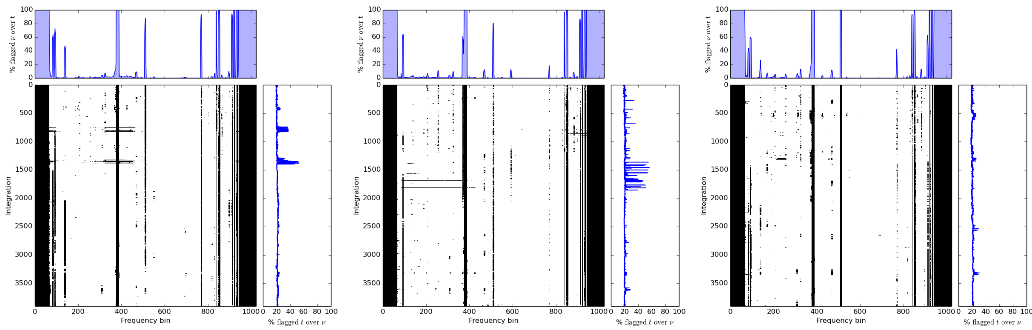

Figure 6.7: *Left to right:* waterfalls of flags for nights 2456732, 2456958 and 2457038. These three nights, along with 2456965, are >20.2% flagged; $> 2\sigma$ above the average flagging amount per night.

a signature of their transmissions[2]. Similar signals were seen on 2456898 (28th August 2014; although only at the beginning of the night) and 2456924 (23rd September 2014). There was no listed orbital or suborbital activity for 2456898. There was an US ICBM test off of the coast of Virginia on 2456924, but this was probably not the cause of the RFI. The flag waterfalls for these nights are shown in Figure **??**.

Another property that the flag waterfalls in Figures 6.7 and 6.8 highlight is the presence of broadband RFI signals, typically present at frequencies lower than the ORBCOMM band. However, while we flagged at the low-end of the band (which had higher noise levels to begin with), it is likely that such broadband pulses dominated the band at those times, and that we failed to flag all of the integrations. Our flagging routine *xrfi_simple.py* does contain a thresholding option for flagging the entire integration given some arbitrary number of frequencies flagged during that integration: some experimentation will be required to decide if that threshold should change.

[2]The internet also suggests... less plausible explanations: `https://www.youtube.com/watch?t=11&v=VtZx8iPO4zs`.

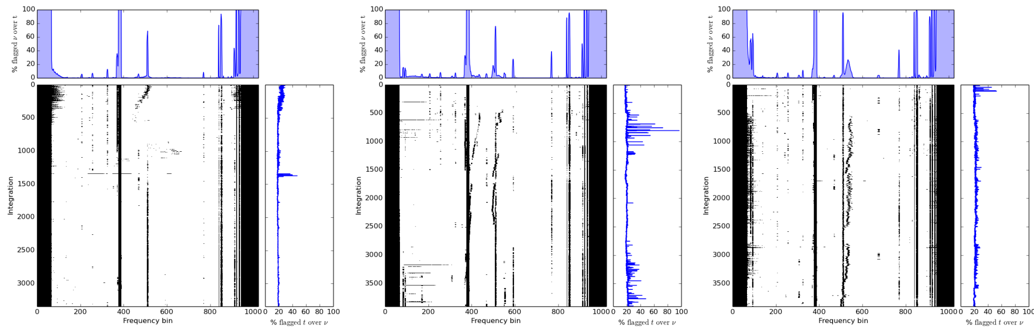

Figure 6.8: *Left to right:* waterfalls of flags for nights 2456898, 2456924 and 2456965. These three nights exhibit a strange behaviour of RFI that changes in frequency and time. JD 2456965 is by far the worst, and during this night as well as 2456898, we see a broadband 'comb' of flagged frequencies near the band edges

6.2.1.3 Discussion

Based on my findings, I was able to recommend some actions that could be taken in the KRQZ to enable better measurements:

- Steps to reduce and ideally eliminate the VHF TV transmissions in the area would be very helpful, since these were clearly interfering with our measurements in the high-end of the band.
- The ISS 149.75±0.55 MHz band should be permanently flagged within the compression pipeline.
- Pursuing re-routing of flight paths will not do much to help: we see aircraft signals for the duration of their flight, not just when they're over the Karoo.
- A lower threshold for identifying broadband RFI should be optimized.

A new, lower-frequency feed is currently under development by the HERA analog group. This would nominally allow measurements to be taken in the range 50–250 MHz, allowing science observations of the Dark Ages and the post-reionization Universe. It should be noted that at the lowest frequencies FM radio will be a constant harassment to these measurements. At the higher frequencies, VHF TV will be the primary contaminant, but should be much easier to remove as it is both narrow-band and within the KRQZ's power to shut off.

6.2.2 HERA-19 and PAPER-19

The HERA-19 IDR1 consisted of four subarrays: the HERA-19 hexagon of dishes (the 'HERA Hex'), a hexagon of 19 PAPER dipoles in the exact positions of not-yet-constructed HERA dishes (the 'PAPER Hex'), an imaging array and an experimental array for polarization measurements. I will concentrate on the two Hexes in this Section. I analyzed RFI as flagged in the linear *xx*-polarization only. Asymmetric beams can in principle receive different RFI events for different linear polarizations, but analysis of that was outside the scope of this diagnostic study.

IDR1 consisted of one 'golden day', JD 2457458. This ran from 6pm on March 10th 2016 to 6am the following day. This gave, per baseline, roughly 4000 integrations of 10 seconds each over 1024, 100 kHz frequency channels from 100 to 200 MHz.

In order to flag RFI I used the `aipy` script *xrfi_simple.py*. I took the union of all baseline flags as data to analyze. Unlike in Section 6.2.1, these data did not have a-priori flagging of band edges, which allowed me to make a more complete study of RFI in the HERA band. I did have to implement custom flags in order to get more than a zeroth-order view of the RFI (since these would dominate the flagging routine unless they are flagged already), but my results from Section 6.2.1 gave a better idea of what was flagged to get there.

Below I present measurements of high-power, mostly narrow-band RFI channels as flagged in HERA Hex data and PAPER Hex data separately. In both cases, I was able to list any channels that are flagged for $\geqslant 1\%$ of the night. I could then compare the flagging Hex-to-Hex, and to PAPER-128.

6.2.2.1 HERA Hex RFI

Table 6.2.2.1 shows all narrowband frequency ranges flagged in HERA-19 visibilities, with columns of the frequency range in MHz, % flagging over time, plausible identification, whether or not it was identified in PAPER-128 data, and other notes (often details of the possible identification). Frequencies with 100% flagging indicate manual flags required for `xrfi_simple` to work on the rest of the channels.

Clearly, the low-end of the band was swamped by FM radio broadcasts. One notable frequency was the 109.2±0.3 MHz band, which was heavily flagged in HERA visibilities, but was only flagged a few percent in PAPER-128 data.

As seen before, ORBCOMM satellite emissions spilled out of their allocated 137-138 MHz band down to 136.3 MHz.

There were many narrowband RFI channels, across the band, that PAPER-128 did not pick-up. Most of these were flagged only at low levels, with two exceptions: 111.3±0.2 MHz and 113.5±0.1 MHz. Both of these were in the aircraft navigation band. There is some evidence (Civil Aviation Authority, 2016) that 111.3 MHz band is fir air force communications. The 113.5 MHz band is a known band for radionavigation beacons ('VOR navaids' World Aero Data, 2016).

A particularly annoying 'new' emitter was in the 153.8±0.2 MHz region, which is close to the center of our nominal EoR band. It could correspond to mobile phones being used close to site.

Table 6.2. RFI as flagged by HERA

ν MHz	Flagged %	Cause (Possible)	Seen by PAPER-128	Notes
100.7 ± 0.2	50	FM Radio	n/a	RSG “Dis Die Een" Prieska
101.5 ± 0.3	36	FM Radio	n/a	RSG “Dis Die Een" Calvinia
102.4 ± 0.1	100	FM Radio	n/a	RSG “Dis Die Een" Carnarvon
102.8 ± 0.3	57	FM Radio	n/a	RSG “Dis Die Een" Pofadder
104.2 ± 0.1	100	FM Radio	n/a	SAfm Prieska
105.1 ± 0.2	100	FM Radio	n/a	SAfm Calvinia
106.2 ± 0.3	100	FM Radio	n/a	SAfm Carnarvon
106.9 ± 0.1	15	FM Radio	n/a	Sentech
107.2 ± 0.1	18	FM Radio	Yes	
107.8 ± 0.2	15	FM Radio	Yes	
108.3 ± 0.1	31	FM Radio?	Yes	
109.2 ± 0.3	93	FM Radio?	Yes...	...but not to this degree
111.3 ± 0.2	25	Air force?	No	
112.5 ± 0.1	5	Aircraft?	No	
113.5 ± 0.1	21	Aircraft	No	VOR navaids
115.5 ± 0.1	3	Navaids?	No	
115.9 ± 0.1	3	Navaids?	No	
116.6 ± 0.2	9	Aircraft?	Yes	VOR-DME navaids
120.1 ± 0.2	5	Aircraft	Yes	CPT$< - >$JNB
125.0 ± 0.2	6	Aircraft	Yes	CPT$< - >$JNB
130.0 ± 0.2	4	Aircraft	No	Communication
131.6 ± 0.2	15	Aircraft	Yes	KLM OPS
136.4 ± 0.1	9	ORBCOMM	Yes	
136.7 ± 0.1	10	ORBCOMM	Yes	
137.4 ± 0.4	100	ORBCOMM	Yes	
145.7 ± 0.4	18	ISS/Amateur Radio band	Yes	
149.9 ± 0.1	100	ISS	Yes	
153.8 ± 0.2	7	Mobile phones?	No	
175.0 ± 0.1	100	VHF TV	Yes	Channel 4 Video
178.3 ± 0.2	8	VHF TV	No	Channel 7?
181.2 ± 0.1	100	VHF TV	Yes	Channel 4 Audio
182.2 ± 0.2	9		Yes	
183.5 ± 0.6	100	VHF TV	Yes	Channel 5 Video
184.1 ± 0.1	2	VHF TV?	Yes	Channel 5?
184.7 ± 0.1	6	Broadcasting	No	
187.8 ± 0.1	4		No	
189.1 ± 0.1	52	VHF TV	Yes	Channel 5 Audio
190.1 ± 0.3	13		n/a	

Table 6.2—Continued

ν MHz	Flagged %	Cause (Possible)	Seen by PAPER-128	Notes
191.1 ± 0.1	100	VHF TV	n/a	Channel 7
197.2 ± 0.2	18		n/a	
199.4 ± 0.5	100	BAND EDGE	n/a	

6.2.2.2 PAPER Hex RFI

Table 6.2.2.2 has the same description as Table 6.2.2.1, but for the PAPER Hex. There were far fewer RFI frequencies flagged in PAPER visibilities, almost all of which were seen by HERA. The only RFI seen by the PAPER Hex and not the HERA Hex was the 123.5±0.1 MHz emission, which I could find a plausible identification for.

6.2.2.3 Hex-to-Hex Comparisons

As mentioned above, the PAPER Hex saw far fewer narrowband RFI channels than HERA does. This highlighted an interesting trade-off between dipoles and dishes: at first glance, one might have expected PAPER dipoles to be more susceptible to RFI given their broader effective beams. However, HERA dipoles are lifted several meters above the ground, and this change in height may have been the source of the greater susceptibility to RFI. RFI comes from the horizon, which would be more easily received in the far sidelobes of the beam.

Even for the RFI channels they did share, HERA flagged them more often. Taking the difference in percentage-flagging for the common RFI channels (think of the left panel subtracted from the right panel for common channels in Figure 6.9), those channels had an average of 8% more flagging in HERA visibilities. The difference was particularly high in the aeronautical radionavigation bands, where HERA had on average 38% more flagging than the PAPER Hex.

Figure 6.10 shows the flags on a per-sample basis (these were averaged over time to

Table 6.3. RFI as flagged by the PAPER Hex

ν MHz	Flagged %	Cause (Possible)	Seen by PAPER-128	Notes
100.0 ± 0.1	100	BAND EDGE	n/a	
100.7 ± 0.1	11	FM Radio	n/a	RSG “Dis Die Een" Calvinia
101.6 ± 0.2	6	FM Radio	n/a	RSG “Dis Die Een" Calvinia
102.4 ± 0.1	100	FM Radio	n/a	RSG “Dis Die Een" Carnarvon
102.7 ± 0.1	100	FM Radio	n/a	RSG “Dis Die Een" Pofadder
104.2 ± 0.2	100	FM Radio	n/a	SAfm Prieska
105.1 ± 0.2	100	FM Radio	n/a	SAfm Calvinia
106.2 ± 0.3	100	FM Radio	n/a	SAfm Carnarvon
108.2 ± 0.1	3	FM Radio?	Yes	
109.1 ± 0.1	26	FM Radio?	Yes	
113.6 ± 0.1	2	Airplane Communications	No	VOR navaid
120.2 ± 0.3	3	Aircraft	Yes	CPT$<->$JNB
123.5 ± 0.1	1		No	Not seen by HERA
125.0 ± 0.2	6	Aircraft	Yes	CPT$<->$JNB
130.0 ± 0.3	3		No	
131.7 ± 0.2	14	Aircraft	Yes	
136.4 ± 0.2	6	ORBCOMM	Yes	
136.7 ± 0.2	6	ORBCOMM	Yes	
137.4 ± 0.4	100	ORBCOMM	Yes	
145.8 ± 0.3	14	ISS/Amateur Radio band	Yes	
149.9 ± 0.1	100	ISS	Yes	
153.8 ± 0.2	3	Single frequency mobile phones?	No	
175.1 ± 0.2	100	VHF TV	Yes	Channel 4 Video
178.3 ± 0.2	100	VHF TV	No	Channel 7?
181.2 ± 0.1	100	VHF TV	Yes	Channel 4 Audio
183.2 ± 0.2	100	VHF TV	Yes	Channel 5 Video
189.2 ± 0.1	100	VHF TV	Yes	Channel 5 Audio
191.2 ± 0.1	100	VHF TV	n/a	Channel 7
199.8 ± 0.2	100	BAND EDGE	n/a	

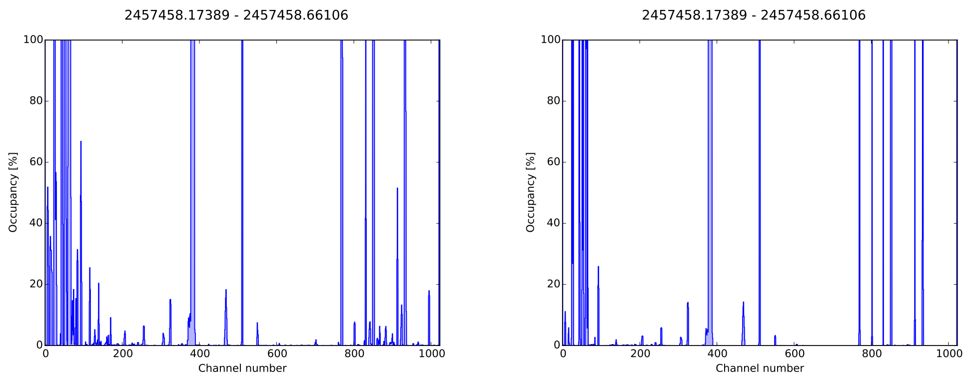

Figure 6.9: Frequency vs. percentage flagging for the HERA Hex (*left*) and PAPER Hex (*right*). Any band with greater than 1% flagging is reported in Tables 6.2.2.1 and 6.2.2.2.

create Figure 6.9). Most apparent was the occupancy of the HERA plot compared to the PAPER Hex one. An important component of this plot is the averages over frequency in the right-hand panels. We saw that the average flagging for a given time sample was about 5% higher for HERA than for the PAPER Hex, mostly due to the higher occupancy of the FM band. But we also saw something new; HERA appeared to be much more sensitive to broadband bursts of RFI. The PAPER Hex caught one of these events (around 1.30am SAST) at high significance, but most of them hardly rose above average flagging. HERA saw five to seven bursts across the night.

6.2.2.4 Comparison PAPER-128 stacked flags

Section 6.2.1 presented RFI flags stacked over 150 days of observations. This method washed-out single events that effect analysis on a single-night basis, but was sensitive to repeatedly offending frequencies. Due to the PAPER-128 analysis pipeline, many channels were automatically flagged (particularly large portions of the band edges), which artificially boosted the average flagging per time and did not allow for closer inspection of the ends of the band. There was some evidence of broadband emission (see Figure 6.2) but the band was largely free of RFI in the middle of the night. Obviously, the data presented in this section shows a less-clean band, but it also only concentrated on a single

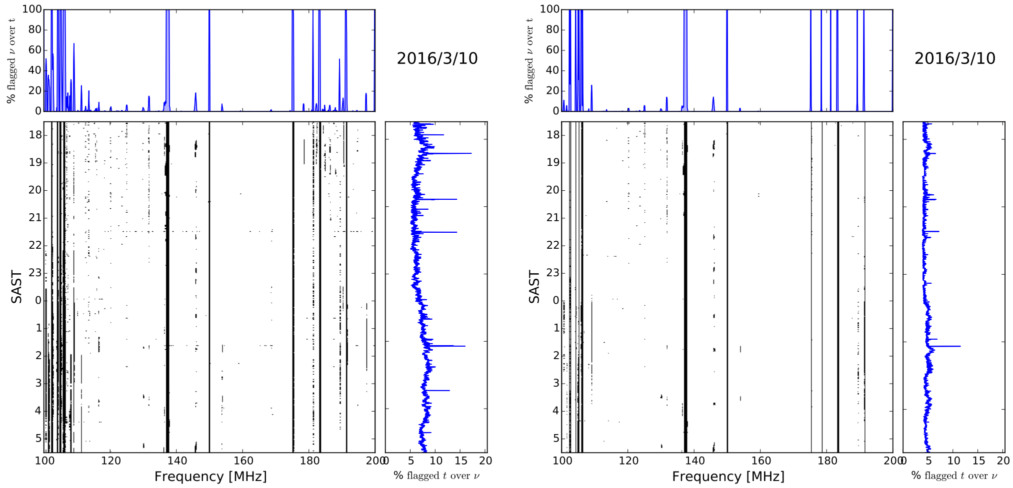

Figure 6.10: RFI flag waterfalls of frequency vs. South Africa Standard Time for the HERA Hex (*left*) and PAPER Hex (*right*). The top panels show the average over time (identical to Figure **??**), while the right panels show the average over frequency.

night's data, so it may be that IDR1 was conspicuous compared to an 'average' night of observations.

Traits shared between the two analyses were:

- Aircraft communications disrupting data until around local midnight.
- ORBCOMM spilling out of it's band.
- VHF TV frequencies emitting throughout the night in the high end of the band.

Table 6.2.2.1 highlighted many frequencies seen by HERA and not by PAPER-128. Again, given the fact that flags were stacked and averaged in Section 6.2.1, these may not have been 'new', but they could have been. Particularly conspicuous were the emissions in the aeronautical radionavigation band.

6.2.2.5 Discussion

I have presented a first look at RFI in HERA-19 Commissioning data. Probably due to the height of the receiving element on HERA versus PAPER dipoles, much more RFI was apparent, especially on the low and high ends of the band. Luckily, the EoR band was largely clean of RFI, except for an emitter at about 154 MHz, which could have corresponded to single-frequency mobile phone communications. Such communications are officially banned in the SKA Radio Quiet Zone (SKA Panel, 2012), which HERA is in the center of.

Only looking at a single night of RFI flags limited the predictive power of this study. More data will be required to establish whether or not this is level of RFI was 'normal'. Broadband RFI bursts require closer investigation.

Efforts to extend the HERA band to lower and possibly higher frequencies are currently under way. The FM radio band extends to around 65 MHz, while the VHF TV band extends to around 230 MHz, so the RFI environment should be a consideration for these efforts.

Meanwhile, I note that the RFI flagging routine used here, `xrfi_simple`, is indeed 'simple'. More advanced RFI flagging algorithms such as `AOFlagger` (Offringa et al., 2012) should be tested in later studies.

6.3 Pre-Redundant Calibration QA

6.4 Post-Redundant Calibration QA

Chapter 7

Polarimetric Calibration

7.1 Redundant Calibration

7.2 Imaging Calibration

Chapter 8

The Ionosphere

The ionosphere is a section of Earth's atmosphere composed of several layers, between 60 and 1000 km in altitude. It overlaps the Troposphere, Stratosphere, Mesosphere, Thermosphere and Exosphere. The ionosphere is an ionized plasma, composed of ions from molecules in the atmospheric layers it overlaps that are ionized by solar radiation. The ionization state of the ionosphere can be quantified by the Total Electron Content (TEC) – an integral of electron count in a given direction – among other metrics.

Spatiotemporal variations of the TEC are tied to solar activity, and therefore largely both diurnal and seasonal. More ionization, and therefore a larger TEC, is to be expected in the day time and closer to the summer solstice. The Solar Cycle also influences TEC, with more sunspots proportional with a higher TEC; at solar maximum, this effect dominates the seasonal variation (Sotomayor-Beltran et al., 2013). Ionospheric variations are typically described as Kolmogorov turbulence (i.e. small scale motions are isotropic in their direction and scale with wavenumber; Zolesi & Cander 2014), however, LOFAR observations report deviations from isotropy in their observations (Intema et al., 2009; Mevius et al., 2016). Regions of the ionosphere that can be assumed to be constant in density and shape at a given time are referred to as "isoplanatic patches". At 74 MHz, these patches are observed to be $1^\circ - 2^\circ$ in radius (Cotton & Condon, 2002).

The ionosphere is composed of three main layers: D, E and F, which vary according to

Table 8.1. Ionospheric Layers

Layer	Time	Altitude km	Components	Electron Density $e^- m^{-3}$
D	Day	60–90	NO^+, N_2, Ar, O_2^-	$10^8 - 10^9$
E	Day/Night	90–150	NO^+, O_2^+, O^+, N_2^+	10^{11}
F_1	Day	140–600	NO^+, O_2^+, O^+, N^+	10^{11}
F_2	Day/Night	220–800	O^+, H^+, He^+	$10^{10} - 10^{13}$

the day-night cycle. These are summarized in Section 8 (which summarizes Chapter 2 of Zolesi & Cander 2014). At night, there are not enough high-energy electrons to penetrate to lower altitudes, causing the D layer to recombine. The E layer increases in altitude at night due to a similar effect. The E and F layers persist at all times, but during daylight the F layer is divided into two sub-layers, F_1 and F_2.

The diurnal nature of the ionosphere is important to radio propagation. During the day, the D layer reflects radio transmissions much closer to the Earth than during the night, when the E and F layers reflect. This leads to longer-range transmissions being possible after sunset[1].

The relevance of the ionosphere to this work is its coupling with Earth's magnetic field. Recall that, as mentioned in previous chapters, a linearly polarized electromagnetic wave, propagating through an ionized plasma which has an incident magnetic field, will experience Faraday Rotation of its original polarization angle χ:

$$\chi_{\text{obs}} = \chi + \phi\lambda^2 \tag{8.1}$$

where λ is the wavelength, and

$$\phi(\hat{s}) \approx 0.81 \int_{\text{source}}^{\text{obs}} n_e(\hat{s})\vec{B}(\hat{s}) \cdot d\vec{s} \tag{8.2}$$

[1]This effect was first observed by E. V. Appleton (Appleton, 1946), confirming the ionosphere's existence, for which he was awarded the 1947 Nobel Prize in Physics.

where the source of the electromagnetic wave is in direction $\hat{s}$ on the sphere, n_e is the electron density scalar field and $\vec{B}$ is the magnetic vector field. The Rotation Measure (RM) ϕ is the integral of the product along the line of sight, and has units of rad m^{-}2. Since the ionosphere is capable of imparting an additional RM to polarized radio waves, inducing spectral structure to interferometric visibilities, understanding it is crucial to quantifying the effect of polarization on EoR measurements.

In this chapter, I review historical measurements of the ionospheric TEC and RM distributions in Section 8.1 and modern observations in Section 8.2. In Section 8.3 I present our work on the role of the ionosphere in PAPER and HERA measurements, and software we developed to quantify those effects.

8.1 Historical measurements of TEC and RMs

The existence and layered nature of the ionosphere was confirmed between the 1920s and the 1940s. Measurements of the TEC and RM distributions came later, once radio-communications satellites were put in orbit, and are closely tied to the Global Positioning System (GPS) launched in the late 1970s (called the NAVSTAR system). NAVSTAR GPS satellites transmit at two narrow frequency bands, centered about 1.2276 GHz (“L_2") and 1.57542 GHz (“L_1"). Encoded in these transmissions are the local clock times per satellite (precisely calibrated with one another and with ground clocks) and their positions. With four satellites in view of a receiver, one is capable of computing their three-dimensional position and their local clock relative deviation from the satellite clock time.

MacDoran & Spitzmesser (1989) showed that one could use a frequency-dependent time delay induced by the ionospheric plasma (Klobuchar, 1983; Brunner & Welsch, 1993):

$$\Delta t_{\text{iono}} = \frac{40.3}{c\nu^2}\text{TEC} \tag{8.3}$$

to calculate an estimate of the TEC in the direction of a GPS satellite. Their approach has been continously refined. Using an estimate of the polarization angle of the emitted $L_{1,2}$ transmissions, Titheridge (1972) and Royden et al. (1984) presented measurements of TEC by measuring the Faraday Rotation induced and worked towards an estimate of the TEC based on the RM. Lanyi & Roth (1988) showed that the more accurate method was calculation of the TEC using $\Delta t_{\rm iono}$ from Equation 8.3. Mannucci et al. (1998) introduced the Ionosphere Map Exchange Format (IONEX): a method and file format for storing TEC measurements using GPS beacons across the globe, allowing the first global TEC maps to be calculated. IONEX files contain global TEC measurements with a 2 hour cadence and generally 5° by 2.5° resolution in longitude and latitude respectively. They neglect the layered nature the ionosphere, modelling it as a thin sheet. Iijima et al. (1999) provided a server that automatically pushed IONEX files to the World Wide Web as soon as they could be constructed. Komjathy et al. (2005) presented the first measurements with over 1000 GPS stations. Recently, Erdogan et al. (2016) presented a method for time-series forward modelling of the TEC distribution using IONEX files.

Meanwhile, many generations of the International Geomagnetic Reference Field (IGRF **?**) have continually improved the model of the Earth's magnetic field. This model is composed by spatial interpolation of magnetic field measurements (in up to 13th-order spherical harmonic coefficients) reported by institutions around the world.

Combining these two measurements – IONEX and IGRF data – can provide a map of RM distribution above any given position on Earth to moderate precision (better in the Northern Hemisphere than the Southern one, based on the number of GPS beacons in each). Afraimovich et al. (2008) offered the first such software implementation, with the objective of using it to track Solar Activity[2]. Sotomayor-Beltran et al. (2013) introduced the `ionFR` package, which calculated ionospheric RMs towards a given position on the sky. We generalized their approach for the wide-field measurements in our `radionopy` software package, which we present in Section 8.3.

[2]Erickson et al. (2001) were the first to present software capable of calculating ionospheric RMs using the IGRF, but they used local GPS beacons instead of IONEX files

8.2 Low frequency observations: discoveries and challenges

Low frequency interferometric observations are effected in two main ways by ionospheric turbulence: scintillation in Stokes I observations, and Faraday Rotation in Stokes Q and U observations.

TEC variations introduce a variable index of refraction across a field of view. Stokes I signal from a point source will scintillate, change position, by an amount (e.g. Thompson et al., 2017):

$$\Delta\theta = -\frac{1}{8\pi^2}\frac{e^2}{\varepsilon_0 m_e}\frac{1}{\nu^2}\nabla_\perp(\mathrm{TEC}) \tag{8.4}$$

at the observed frequency ν, where $\nabla_\perp$ is the transverse gradient in TEC towards the direction of the source. The time, space and frequency dependence of this effect causes difficulty for long integrations, since the scintillation will cause averaging of point sources with empty space, spreading-out their signal over a $\sim \Delta^2\theta$ area. This can be interpreted as an additional source of noise in a Stokes I map. Vedantham & Koopmans (2015) showed that this scintillation noise can be much larger than image noise for baselines longer than ~ 200 m. Vedantham & Koopmans (2016), extending the previous analysis to the Fourier domain, showed that this noise does not pose large issues to HERA or SKA-Low EoR efforts, since realistic amounts scintillation were not sufficient to wash-out EoR signals on large scales (their dense cores of relatively short baselines also help). However, it could pose large issues for point-source calibration and subtraction methods – as emphasized in a public SKA memo by Cornwell (2016).

Loi et al. (2015) used MWA observation snapshots to map the scintillation as a function of space and time, resulting in the discovery of “tubes" of plasma density waves across the Southern Hemisphere in lines of roughly constant latitude. Comparing the sources in their snapshot images to source positions in the NRAO VLA Sky Survey (NVSS Condon et al., 1998) they were able to calculate displacement vectors, and showed that they were strongly aligned to Earth's magnetic field.

The literature surrounding ionospheric Faraday Rotation is less extensive than work focussing on the unpolarized component. Lenc et al. (2016) showed that MWA measurements of diffuse foregrounds could provide a map of ionospheric spatiotemporal variance as their RM changed throughout a series of observations. Lenc et al. (2017) showed that point source power could be seen "twinkling" in and out of polarized intensity maps due to ionospheric activity.

8.3 Relevance for PAPER and HERA EoR measurements

Within the PAPER and HERA power spectrum pipelines, many tens to hundreds of days of visibilities are averaged over during binning in LST. The the ionosphere-induced spatial and temporal fluctuations in RM could produce sufficient phase scrambling of the celestial Faraday-rotated, polarized signal to suppress a fraction of any polarized signal leaked by some mechanism into Stokes I measurements. The fringe size of the 30 m baselines used in power spectrum analyses is large enough that scintillation effects are negligible.

This effect was first investigated in Moore et al. (2017). Using the `ionFR` package (Sotomayor-Beltran et al., 2013) we calculated the RM distribution at a single zenithal pointing throughout the PAPER-32 observation season. This was a vast simplification given the PAPER primary beam was much larger than a typical isoplanatic patch. Shown in Figure 8.1, there was a large spread of ionospheric RMs for each LST. There was a decrease in the average magnitude of the RM as LST increased. This was expected, given the strong correlation between the day/night cycle and TEC values (e.g. Tariku, 2015), and given that for this observing season, LST=4 hr corresponded to observations taken shortly after sunset, while LST=8 hr was always well into the night.

Treating the single pointing as constant over the sky, we calculated the expected attenuation of polarized signal, leaked into pseudo-Stokes I visibilities, that would be averaged over varying ionospheric conditions during LST binning. These attenuation factors were

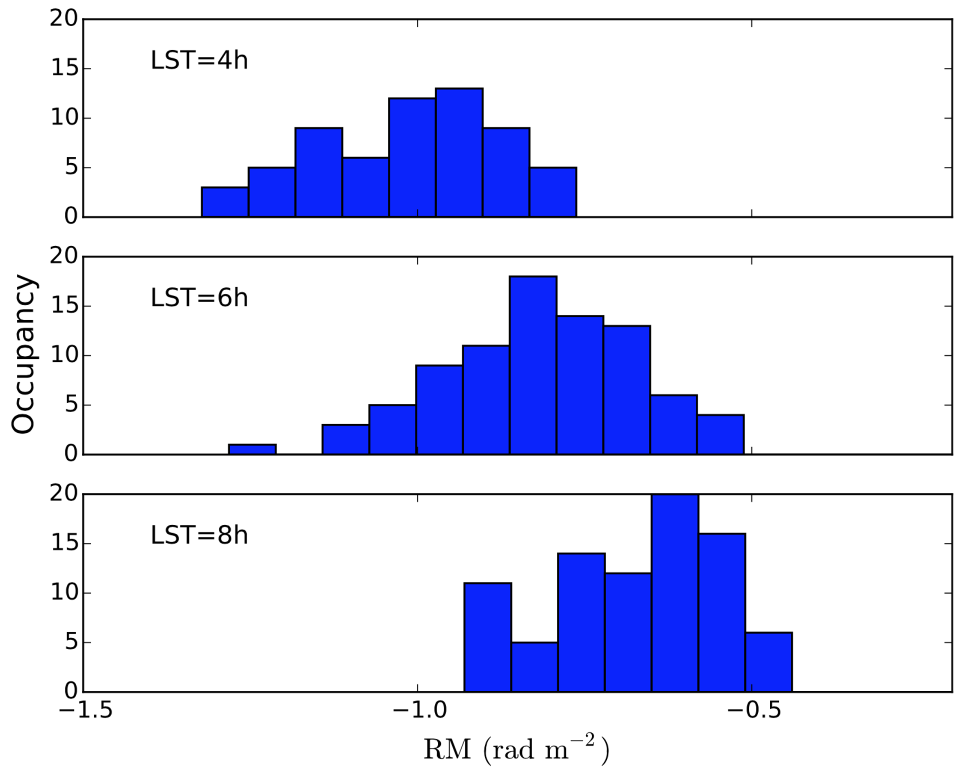

Figure 8.1: Distribution of zenithal ionospheric RMs for 3 LSTs in the PAPER-32 observing season. From top to bottom: a histogram of the zenith ionospheric RMs over the season, for the transit of LSTs 4, 6, and 8 hr. Taken from Moore et al. (2017).

43±6% at 165 MHz and 7±5% at 126 MHz.

To build on this result, we required more sophisticated simulations of the interaction of the polarized sky with the instrument and whole-sky maps of the ionosphere. To accomplish the latter, we developed the open-source Python package `radionopy`[3]. Like `ionFR`, `radionopy` uses GPS-derived TEC maps from IONEX files and the IGRF to estimate the value of ionospheric RM at a given latitude, longitude and date. Unlike its predecessor, `radionopy` does not necessarily calculate an RM at a given pointing, but instead is capable of calculating the ionospheric RM over a `HEALPix` grid of the sky (**?**). Such an expression of ionospheric variation is natural to wide-field, drift-scanning EoR arrays, and reflects the format of the IONEX input measurements, which are given in their spherical harmonic decompositions. `radionopy` is vectorized, leading to efficient generation of full-sky ionospheric maps, and object-oriented, allowing for easier collaborative development. Additionally we implemented the interpolation scheme recommended in the IONEX documentation to obtain "best-guess" full-sky maps for arbitrary times between the 2-hour time resolution of IONEX data.

An example output from `radionopy` is shown in Figure 8.2 as a HEALPIX grid of the hemisphere observable from the PAPER site in the Karoo. In Figure 8.3 we show `radionopy` and `ionFR` output for a single pointing towards Cassiopeia A (Cas A; RA=$23^{\mathrm{h}}23^{\mathrm{m}}27.9^{\mathrm{s}}$, Dec=$+58°48'42.4''$) from the LOFAR Core site in the Netherlands. The two codes gave qualitative agreement. Slight offsets at the highest RM values that day could be attributed to differences in our interpolation schemes.

Martinot et al. (in prep.) investigated the full interaction of the polarized sky with the ionosphere, using realistic polarized sky models and fully-polarized HERA beam models (see Chapter 10 for an example). Their work revealed that the Moore et al. (2017) analysis overestimated the ionospheric attenuation due to their single-pointing and simple beam models. Realistic levels of attenuation for a 100 day HERA integration can be expected to reach a factor of $\leqslant 0.1$. If polarization leakage occurs close to the EoR level, this is

[3] `https://github.com/UPennEoR/radionopy`

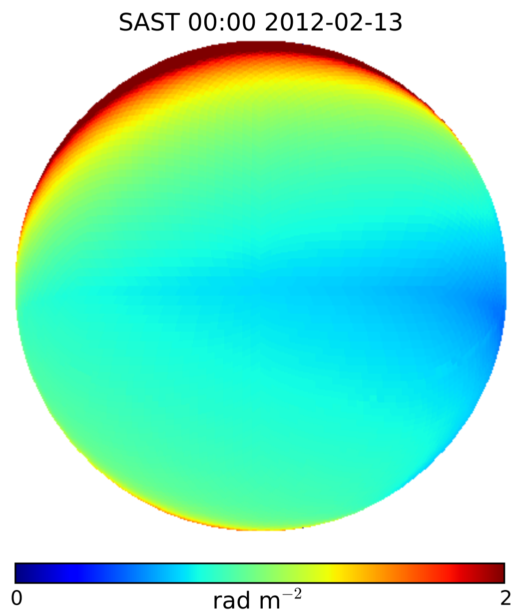

Figure 8.2: An example of widefield ionospheric RMs calculated by `radionopy`.

sufficient to recover the EoR power spectrum. However, if it is above the EoR level (as expected by Nunhokee et al. 2017), the ionosphere alone will not be sufficient to rule out polarization leakage being detected before the EoR can be recovered.

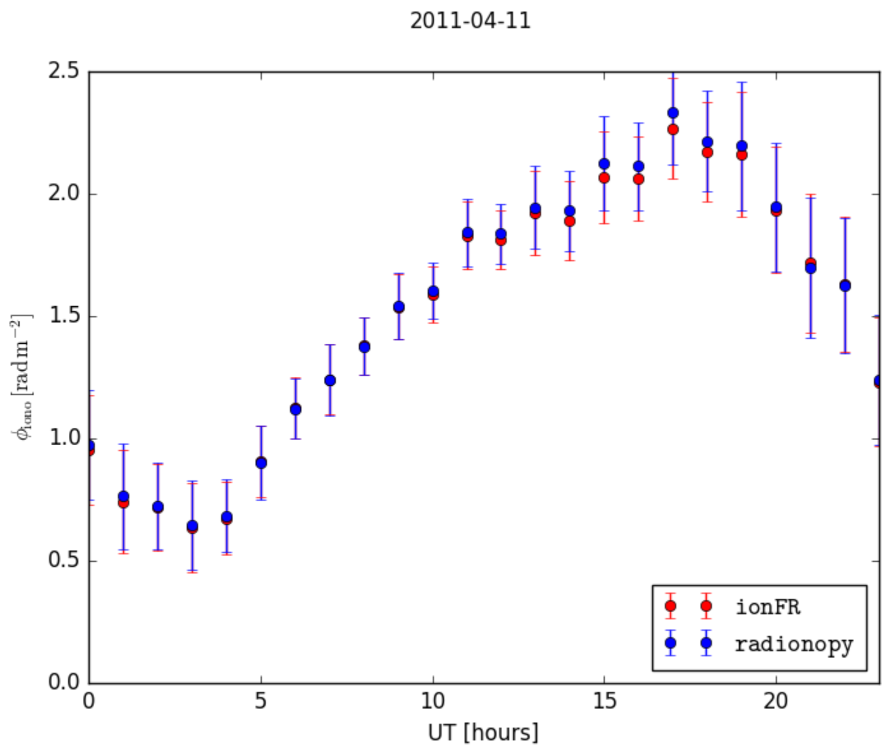

Figure 8.3: The RM of Cas A as viewed from the LOFAR Core site in the Netherlands on April 11th, 2011, according to `ionFR` and `radionopy`. The two codes show quantitative agreement, demonstrating that radionopy can be used for single-pointing as well as full-sky RM measurements.

Chapter 9

A view of the EoR window from the PAPER-32 imaging array

In this Section, we present 2D power spectra created from data taken by the PAPER-32 imaging array in Stokes I, Q, U and V.

The PAPER 32-antenna array relied on its highly redundant configuration in order to take the measurements resulting in the strong upper limits on the 21 cm power spectrum (Parsons et al., 2014; Jacobs et al., 2015; Moore et al., 2017). However, for three nights in 2011 September, the 32 elements were reconfigured into an polarized imaging configuration. Creating power spectra allowed us to observe and diagnose systematic effects in our calibration at high signal-to-noise within the Fourier space most relevant to EoR experiments. We observed well-defined windows in the Stokes visibilities, with Stokes Q, U and V power spectra sharing a similar wedge shape to that seen in Stokes I. With modest polarization calibration, we saw no evidence that polarization calibration errors moved power outside the wedge in any Stokes visibility, to the noise levels attained. Deeper integrations will be required to confirm that this behavior persists to the depth required for EoR detection.

The layout of this Chapter is as follows. In Section 9.1 we provide a brief description of the PAPER array in its imaging configuration, the data from which this paper is based, and describe its calibration and reduction. We also describe the method used to create 2D power spectra in this section. We analyze the power spectra in Section 9.2, and discuss the implications of our findings and conclude in Section 9.3.

9.1 Observations & Reduction

We present measurements taken overnight on 2011 September 14–15 over local sidereal times (LSTs) 0–5 hr.

Antennae were arranged in a pseudo-random scatter within a 300 m-diameter circle, the layout of which is shown in Figure 9.1. This allowed us to obtain resolutions between 15' and 25' across the bandwidth (100–200 MHz nominally, although in reality this extends 110–185 MHz due to band edge effects and VHF TV). Drift-scan visibilities were measured every 10.7 s, and divided into datasets about 10 minutes in length. We express an interferometric visibility V_{ij}^{pq} between antennae i (with dipole arm p, which can be x (East-West) or y (North-South) for PAPER dipoles), and j (with dipole arm q), in directional cosines l and m for frequency ν at time t, as:

$$V_{ij}^{pq}(\nu,t) = g_i^p g_j^{q*} \exp(-2\pi i\nu\tau_{pq})\times \int d\Omega A^{pq}(\Omega,\nu) S(\Omega,\nu) \exp\left(\frac{-i\nu}{c}\vec{b}(t)\cdot\hat{s}(\Omega)\right) \tag{9.1}$$

where the g terms represent the complex gains for each antenna and dipole arm, A^{pq} is the polarized beam and S is the sky. The product $\vec{b}(t)\cdot\hat{s}(\Omega)$ represents the projection of the baseline between i and j with respect to an arbitrary location on the sky. The motivation for including the term for the delay between dipole arms p and q, τ_{pq}, is given in Section 9.1.1.3. This delay is clearly zero if $p = q$.

Visibilities were obtained from correlating both x and y dipoles, forming V^{xx}, V^{xy}, V^{yx} and V^{yy}. Frequencies from 100 to 200 MHz were sampled into 2048 channels. Data were delay-filtered to 203 frequency channels (see the Appendix of Parsons et al., 2014) and Chapter 6. Cross-talk was modelled and removed by subtracting the average power over

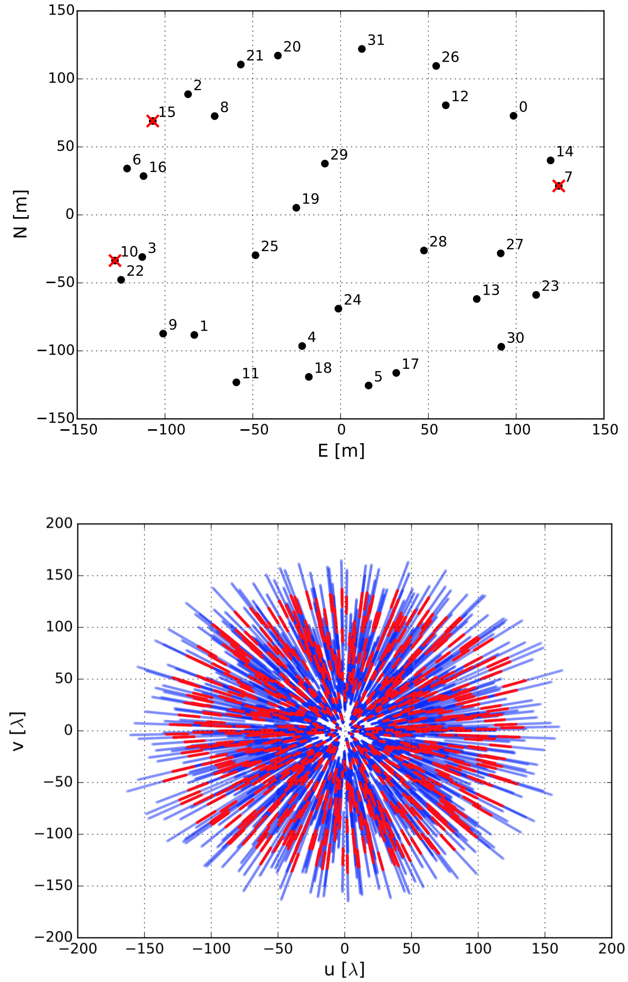

Figure 9.1: The PAPER-32, dual-pol antenna imaging configuration (top). They were arranged in a pseudo-random scatter within in a ∼300 m diameter circle to maximize instantaneous *uv* coverage (bottom). *uv* coverage is shown for 100–200 MHz over 203 channels in blue, and 146–166 MHz over 20 channels in red (the latter being the frequencies used in our power spectrum analysis). Malfunctioning antennae identified during calibration are overlaid with red crosses (and are excluded from the *uv* coverage map).

the 5 hours of observation, which extended across LST=0h–5h. An initial RFI-flagging removed any outliers more than 6σ from a spectrally smooth profile.

9.1.1 Calibration

Calibration took place in three stages, detailed below: a first-order delay-space calibration for the initial gains and phases with respect to Pictor A, an absolute calibration using imaging with respect to Pictor A and Fornax A, and a polarimetric correction for the τ_{xy} phase term in the V^{xy} and V^{yx} visibilities. Traditional polarimetric calibration proceeds by observing a source with a known polarization angle, and solving for up to seven direction-independent terms in the Jones matrix (e.g. Thompson et al., 2017; Hamaker et al., 1996), as well correcting for the effects of the primary beam. Given the dearth of suitable calibrators at our observing frequencies, especially at the relatively low resolution and sensitivity of the array, we proceeded with polarized calibration using different techniques, as described in Section 9.1.1.3 below.

9.1.1.1 Initial calibration

A first-order gain and phase calibration was performed by a similar approach to Jacobs et al. (2013). Each 10 minute drift-scan dataset was phased to the known position of Pictor A using `aipy` routines.

The gain term in Equation 9.1 was approximated as

$$g_i^p = G_i^p \exp(-2\pi i\nu\tau_{ip}) \tag{9.2}$$

and the required delay τ_{ip} offset of the uncalibrated delay tracks to the real position on the sky solved for to obtain a phase calibration; the absolute flux calibration G_i^p was found by isolating the tracks of Pictor A in delay space, and applying the required flux scale across the band (for a discussion of delay-space calibration, see Parsons et al., 2012b, and Figure 9.4).

9.1.1.2 Absolute Calibration

Visibilities were converted to `CASA` Measurement Sets to be further calibrated using a custom pipeline developed around `CASA` libraries. Snapshot images were generated for each 10 minute observation by Fourier transforming the visibilities. We used uniform weights and the multi-frequency synthesis algorithm to further improve the *uv* coverage. Dirty images were deconvolved down to a 5 Jy threshold using the Cotton-Schwab algorithm. The sky model generated by the CLEAN components was used to self-calibrate each snapshot over the full bandwidth, using a frequency-independent sky-model and averaging over the 10 minute observation. We corrected for residual cable length errors by computing antenna-based phase solutions for each frequency channel for each snapshot observation. After self-calibration, snapshot visibilities were again Fourier transformed into images and deconvolved down to a 2 Jy threshold to form the final sky models. These final sky models were used to solve for a frequency independent, diagonal, complex Jones matrix (Hamaker et al., 1996; Smirnov, 2011) for each antenna in order to calibrate gain variations from snapshot to snapshot. We make no attempt to correct sky models for polarized primary beams and, therefore, our gain solutions incorporate both the direction independent and the direction dependent responses of the two gain polarizations. This is a reasonable approximation for the scope of the paper, as, eventually, wide-field polarization corrections cannot be implemented directly in the per-baseline power spectrum estimation (see Section 9.2).

The average correction in magnitude through this second-order calibration was a $\pm 6\%$ change for x gains and $\pm 7\%$ for y gains from those derived in the initial delay-space calibration. If the gain on an antenna deviated by more than 30% from image-to-image during this analysis, it was discarded from future processing stages, since it was likely malfunctioning. This was true for 3 antennae (see the top panel of Figure 9.1).

The final gain amplitude calibration was carried out similarly to Ali et al. (2015). We generated single channel images between 120 and 174 MHz for each snapshot and deconvolved each of them down to 10 Jy. For each snapshot, a source spectrum is derived for Pictor A by fitting a two dimensional Gaussian the source using the `PyBDSM`[1] source extractor (Mohan & Rafferty, 2015). Spectra were optimally averaged together

[1] `http://www.lofar.org/wiki/doku.php?id=public:usersoftware:pybdsm`

by weighting them with the primary beam model evaluated in the direction of Pictor A. To fit the absolute calibration, we divided the model spectrum (Jacobs et al., 2013) by the measured one and fit a 6th order polynomial over the 120-174 MHz frequency range. This procedure was repeated using Fornax A with the only difference that a taper was applied to the visibilities (120 m) in order to reduce Fornax A to a point-like source and use the model spectrum from Bernardi et al. (2013). The best fit coefficients for Pictor A and Fornax A were averaged together to obtain the final absolute flux density calibration. Snapshots of fully CASA-calibrated data are shown in Figure 9.2.

9.1.1.3 Polarimetric factors

Standard full polarization calibration involves correcting for leakage of Stokes I into the V_{ij}^{xy} and V_{ij}^{yx} visibilities and leakage of polarized signal into total intensity (the so called Jones D matrices or D-terms; e.g. Thompson et al. (2017); Hamaker et al. (1996)), and an unknown phase difference between the x and y feeds (e.g. Sault et al., 1996).

We attempt no D matrix calibration in this paper, as there is not a dominant source to be used for such calibration: the limited sensitivity of our observations does not offer good signal-to-noise ratio on PMN J0351-2744, the only polarized source at low frequencies known so far in our survey area. In addition, D-term calibration would require determination of the primary beam Mueller matrices beyond our current accuracy. The consequences of this limitation are discussed in the analysis of our power spectra in Section 9.2.

As a intermediate measure compatible with these limitations, we therefore adopted a minimization of the phase difference between the V_{ij}^{xy} and V_{ij}^{yx} visibilities, minimizing a sum of squared weighted residuals w:

$$w(\nu, t, \tau_{xy}) = \sum_{ij} |V_{ij}^{xy} - V_{ij}^{yx} \exp(-2\pi i \nu \tau_{xy})|^2 \tag{9.3}$$

to find an estimated value of τ_{xy} for the array at each (ν, t) sample. This is equivalent to assuming that the sky is intrinsically not circularly polarized at the frequencies observed by PAPER.

We choose not to correct for ionospheric Faraday rotation in our calibration. Not only is this difficult to do for widefield instruments, but also the ionosphere was relatively stable during the observations, so we expect little incoherent averaging during the power spectrum stage below. We calculated the stability of ionospheric RM ($\phi_{\rm iono}$) using the IONFR software (Sotomayor-Beltran et al., 2013), which calculates the $\phi_{\rm iono}$ for a given longitude, latitude and time by interpolating values of GPS-derived total electron content maps and the International Geomagnetic Reference Field (Finlay et al., 2010). The values of $\phi_{\rm iono}$ for different lines of sight are shown in Figure 9.3. Fluctuations of $\phi_{\rm iono}$ will cause incoherent time-averaging and subsequent loss of polarized signal. Using the formalism of Moore et al. (2017) to calculate the attenuation factor, we found that none of the lines of sight (except for the 21h,0° one which goes beneath the horizon) shown are responsible for attenuating signal by $> 20\%$ in power-spectrum space (see Section 9.1.2).

We form linear combinations of the instrument visibilities, the so-called pseudo-Stokes visibilities (see e.g. Moore et al., 2013) V^I, V^Q, V^U and V^V as:

$$\begin{pmatrix} V^I \\ V^Q \\ V^U \\ V^V \end{pmatrix} = \begin{pmatrix} 1 & 0 & 0 & 1 \\ 1 & 0 & 0 & -1 \\ 0 & 1 & 1 & 0 \\ 0 & -i & i & 0 \end{pmatrix} \begin{pmatrix} V^{xx} \\ V^{xy} \\ V^{yx} \\ V^{yy} \end{pmatrix} \tag{9.4}$$

Data that were reduced, calibrated, and formed into Stokes visibilities were separated into delay spectra inside and outside of the horizon for each baseline. We used a 50 ns margin for what was considered 'inside' the horizon, in order to confine all supra-horizon emission (e.g. Parsons et al., 2012b; Pober et al., 2013) to the foreground component of the data. We implemented a one-dimensional CLEAN (Parsons & Backer, 2009; Parsons et al., 2012a) with a Blackman-Harris window to a tolerance of 10^{-9}. RFI is more easily identified in foreground-removed data, so we RFI-flagged again on the background data deviations greater than 3σ. We then added the inside- and outside-horizon visibilities back together; RFI flags were preserved in the process.

The effect of our calibration is shown in the delay-transformed visibilities in Figure 9.4. As is apparent in Figure 9.2, after improved calibration there are fewer delay tracks (i.e. sources) in the Stokes Q visibilities, while there is little overall change in Stokes U. The minimization of Stokes V, performed after the imaging calibration stage, moves power from Stokes V into Stokes U, effectively accounting for part of a *D*-term correction. But without an accurate *D*-term calibrator, Stokes U exhibits additional (and dominant) *D*-term leakage from Stokes I, in this case due to Pictor A. Pictor A is the brightest source in Stokes I in our observed field, and thus dominates the visibility shown. There is no reason to suppose that Pictor A is pure Stokes U (compare also Figure 9.2), and thus the bulk of this emission must be leakage.

9.1.2 Creating power spectra

Expressing the visibility $V_{ij}^{pq}(\nu,t)$ observed at time t (see Equation 9.1) in terms of the geometrical delay $\tau_g = \vec{b}(t)\cdot\hat{s}(l,m)/c$ for the baseline ij, Parsons et al. (2012b) define the delay transform as the Fourier transform of the visibility along the frequency axis:

$$\tilde{V}_{ij}^{pq}(\tau,t) = \int d\nu\, V_{ij}^{pq}(\nu,t)e^{2\pi i\nu\tau} \tag{9.5}$$

We can represent the power at each frequency and baseline in an array as a power spectrum in terms of their respective Fourier components $k_{\|}$ and $k_{\perp}$ as:

$$P(k_{\|},k_{\perp}) \approx |\tilde{V}_{ij}^{pq}(\tau,t)|^2 \frac{X^2Y}{\Omega B}\left(\frac{c^2}{2k_B\nu^2}\right)^2 \tag{9.6}$$

where B is the bandwidth, Ω is the angular area (i.e. proportional to the beam area), and X and Y are redshift-dependent scalars calculated in Parsons et al. (2012a).

To form $|\tilde{V}_{ij}^{pq}(\tau,t)|^2$, consecutive integrations were cross-multiplied, phasing the zenith of latter to the former i.e.:

$$|\tilde{V}_{ij}^{pq}(\tau,t)|^2 \approx |V_{ij}^{pq}(\tau,t)\times V_{ij}^{pq}(\tau,t+\Delta t)e^{i\theta_{ij,\mathrm{zen}}(\Delta t)}|^2 \tag{9.7}$$

where Δt=10.7 seconds and $\theta_{ij,\mathrm{zen}}(\Delta t)$ is the appropriate zenith rephasing factor. This method should avoid noise-biased power spectra except on very long baselines, which the PAPER configuration does not contain, while sampling essentially identical k-modes. Note that this is the same method used by Pober et al. (2013) in their investigation of the unpolarized wedge.

9.2 Results

Combining visibilities using Equation **??**, we formed power spectra over frequencies 146–166 MHz according to Equation 9.6 using consecutive integrations for each Stokes visibility over time, and gridded our results into k-space, averaging in time. The $k_\perp$-axis is binned with a resolution of $4.65 \times 10^{-4}\,h\,\mathrm{Mpc}^{-1}$ to slightly reduce gaps in k-space due to missing baselines. This gave an average bin occupancy of 1.7±0.9. The resolution in $k_\parallel$ ($5.06 \times 10^{-4}\,h\,\mathrm{Mpc}^{-1}$) is set by the 20 MHz bandwidth with 500 kHz resolution that we use in this analysis. Note that the Blackman-Harris window used in the delay-filtering stage after forming Stokes visibilities correlates adjacent frequency bins, and hence $k_\parallel$ bins. Each $(k_\perp, k_\parallel)$ bin was normalized by its occupancy.

Two-dimensional power spectra have been proven as powerful tools for large dipole array experiments, not only for assessing cosmology but also in order to constrain instrumental and analytical systematics (e.g. Morales et al., 2012). Polarization axes are a useful addition for such analyses, since we expect Stokes I to be approximately 3 orders of magnitude stronger than the other polarization products at the low radio frequencies and tens-of-arcminute scales native to PAPER observations (e.g. Pen et al., 2009; Moore et al., 2013) and when observing far from the Galactic Plane. This alone allows us to assume that much of the structure in the power spectra with power comparable to Stokes I is leakage. As we explore below, these leakage terms can come from direction-dependent effects (e.g. wide-field beam leakage; Carozzi & Woan, 2009) or direction independent ones (e.g. Mueller matrix mixing via gain errors and D-terms; Thompson et al., 2017) and appear with high signal-to-noise in power spectra.

Figure 9.5 shows power spectra in 'pitchfork' form (Thyagarajan et al., 2015b,a), with

$k_{\|}$ in negative and positive directions (according to the East and West horizons, marked in white (horizon) and orange (horizon+50 ns delay, respectively). Each Stokes parameter pitchfork has its own interesting characteristics, which allow us to analyze different sky and instrument behaviors. The 'wedges' described in the literature that define the EoR window are simply the average of negative and positive values of $k_{\|}$. While we focus on the pitchfork expression of the power spectra in our results, we also show them in wedge form in Figure 9.6[2].

Simplifying the results of Thyagarajan et al. (2015b,a, see their papers for a full discussion), we expect power from diffuse emission to appear at low values of $k_{\perp}$ and high values of $k_{\|}$, while point sources lie at all $k_{\|}$ (all over the sky) but are down-weighted by the primary beam, which is broad, leaving a concentration of the power close to the $k_{\|} = 0$ line.

In Stokes I, we see the strongest power on most baselines arising at values $k_{\|} \approx 0$. This is expected in a situation of point sources that are relatively bright compared to any diffuse emission. Indeed, at the LSTs we observed at, several unresolved bright point sources transit the field (e.g. Figure 9.2), while the dominant source of diffuse emission at these frequencies, the Galactic plane, was below the horizon. However, we do see strong super-horizon emission at $0.02 \leqslant k_{\perp} \leqslant 0.03$, biased towards negative $k_{\|}$ values. There is also a decrease in power with increasing $k_{\perp}$ – both of these effects are consistent with the Thyagarajan et al. (2015a) simulations of faint diffuse structure transiting zenith.

The Stokes Q wedge shows a concentration of power close to $k_{\|} \approx 0$, similar to Stokes I. The inherent low polarization fraction at our frequencies works in our favor in detecting gain errors, since Stokes Q is largely expected to be faint, and thus the gain errors causing leakage from I appear at high signal-to-noise there. Indeed, this power decreases noticeably with more accurate gain amplitude calibration, but bright streaks at specific values

[2]Note the difference in the power distribution within the horizon differs from that shown in the Pober et al. (2013) V^{yy} wedge. That study used the PAPER 64-element, single-polarization imaging array to create power spectra in a 'loud' field containing point sources and Galactic signal, causing their wedge to be 'fuller' than the ones presented in this study.

of $k_\perp$ remain, suggesting lower-level residual gain calibration errors on select baselines. Another possible source of power in Stokes Q stems from wide-field direction-dependent gain errors causing a non-smooth evolution of the sources on the edges of the beam. However, we would expect this effect to be biased towards horizon values of $k_{||}$.

Power appears distributed in 'pockets' in the Stokes U power spectrum, not strongly correlated with the distribution of power in I. Stokes I is able to leak into Stokes U via *D*-term leakage (Thompson et al., 2017; Geil et al., 2011), which could occur at any post-amplification stage of observations, such as in cables or receivers. These leakages would be direction independent, and therefore uncorrelated in *k*-space. Such a mechanism could explain the behavior within Stokes U wedge. Before absolute calibration, similar structure is seen in the Stokes V power spectrum.

At these frequencies, Stokes V is thought to be intrinsically zero, with few exceptions. However, Hamaker et al. (1996) show that antennae rotated with respect to one another can produce erroneous Stokes V power via I$\rightarrow$V leakage.[3] This effect may explain some of the small pockets of power that remain in the Stokes V power spectrum after absolute calibration, although such an effect is also consistent with *D*-term leakage. The fact that power within the horizon was greater than the noise level may also have been due to I $\rightarrow$ V leakage through the primary beam.

The relationship between polarizations is highlighted in Figure 9.7. We show a slice of the wedges over $0.097 < k_\perp < 0.098\,h\mathrm{Mpc}^{-1}$ ($\sim$175 m) for Stokes I, Q, U and V (right panels) and the average power over these slices as a function of $k_{||}$ (left panel). The standard deviations for each Stokes parameter are shown as dotted lines. Dashed vertical lines show the horizon at $k_\perp$=0.097 (left) and super-horizon at $k_\perp$=0.098 (right).

A heartening aspect of Figure 9.7, and indeed all of the power spectra in this work, is that the power in Stokes Q, U and V proves to be just as confined within the horizon

[3]It should be noted that while such an error could plausibly have been made in the antenna placement for this imaging array, it is extremely unlikely that it would be made in the redundant PAPER configuration for EoR seasons. In these cases, the antennae were positioned to sub-cm accuracy.

as Stokes I. Whether the polarized Stokes parameters are due to real polarization or miscalibration, not enough spectral structure is being introduced to move emission into the EoR window. Outside of the horizon, Stokes I, Q and U are consistent with the noise level expected for this range of k-modes ($P_{\text{noise}} \sim 10^9$ mK^2(h^{-1}Mpc)^3), according to the formalism Parsons et al. (2012a) and assuming a system temperature $T_{\text{sys}} = 450\,\text{K}$ (e.g. Moore et al., 2017).

9.3 Discussion and Conclusions

We have presented measurements of instrumental polarization leakage in PAPER-32 using 2D power spectra. These have allowed us to quantify some of the possible instrumental effects that could limit a statistical detection of the EoR within the wedge, diagnosed in the Fourier space most relevant EoR statistical detection experiments. To our knowledge, this is the first study of Q, U and V 2D power spectra at these k-modes. We have shown that power from Stokes Q, U and V is as confined to the wedge as Stokes I. Any calibration errors do not appear to spread power outside the horizon.

In their study of 2D power spectra, Asad et al. (2015) reported evidence of polarized leakage into the EoR window at the sub-percent level, considering a 4° degree field of view. Their study differs from this work not only over the field of view (4° versus almost whole-sky), but also in the observing mode (tracked versus drift scan) and in the different k-space probes by LOFAR's longer baselines. In this work the power spectrum is calculated on a per-baseline basis, whereas their study calculates power spectra for gridded data which are more prone to mode mixing effects (Hazelton et al., 2013).

Our results are expected, in principle, to be more prone to leakage contamination due to the intrinsic extremely wide field of view of the PAPER primary beams, however, we see no evidence of leakage in the EoR window down to our sensitivity limits even without correction for polarized beams that is instead included in Asad et al. (2015). Our analysis indicates therefore that neither intrinsic polarized emission nor the PAPER primary beam are leaking power in the EoR window, although longer integrations are required to demonstrate that this is true down to the sensitivities required for EoR detection.

We showed that systematics can be probed with high signal-to-noise using 2D polarized power spectra, using the inherently low polarization fraction at the frequencies PAPER observes at to our advantage. We found that gain errors on specific baselines were easily probed using Stokes Q power spectra. Gain errors appear as continuous streaks within the horizon at specific values of $k_\perp$, allowing us to diagnose the precision of the gain calibration on a per-baseline basis. This is much more difficult to do with only Stokes I power spectra in a non-redundant array, and can be accomplished quickly without imaging. While the features in the Stokes U power spectra are more difficult to attribute to specific baselines, they appear to be consistent with direction-independent leakage. Stokes V power is slightly higher than noise-level within the horizon, suggesting a small but unaccounted-for leakage term from Stokes I, an effect which was explored Nunhokee et al. (2017) – and found to be consistent with beam-leaked signal from Stokes I.

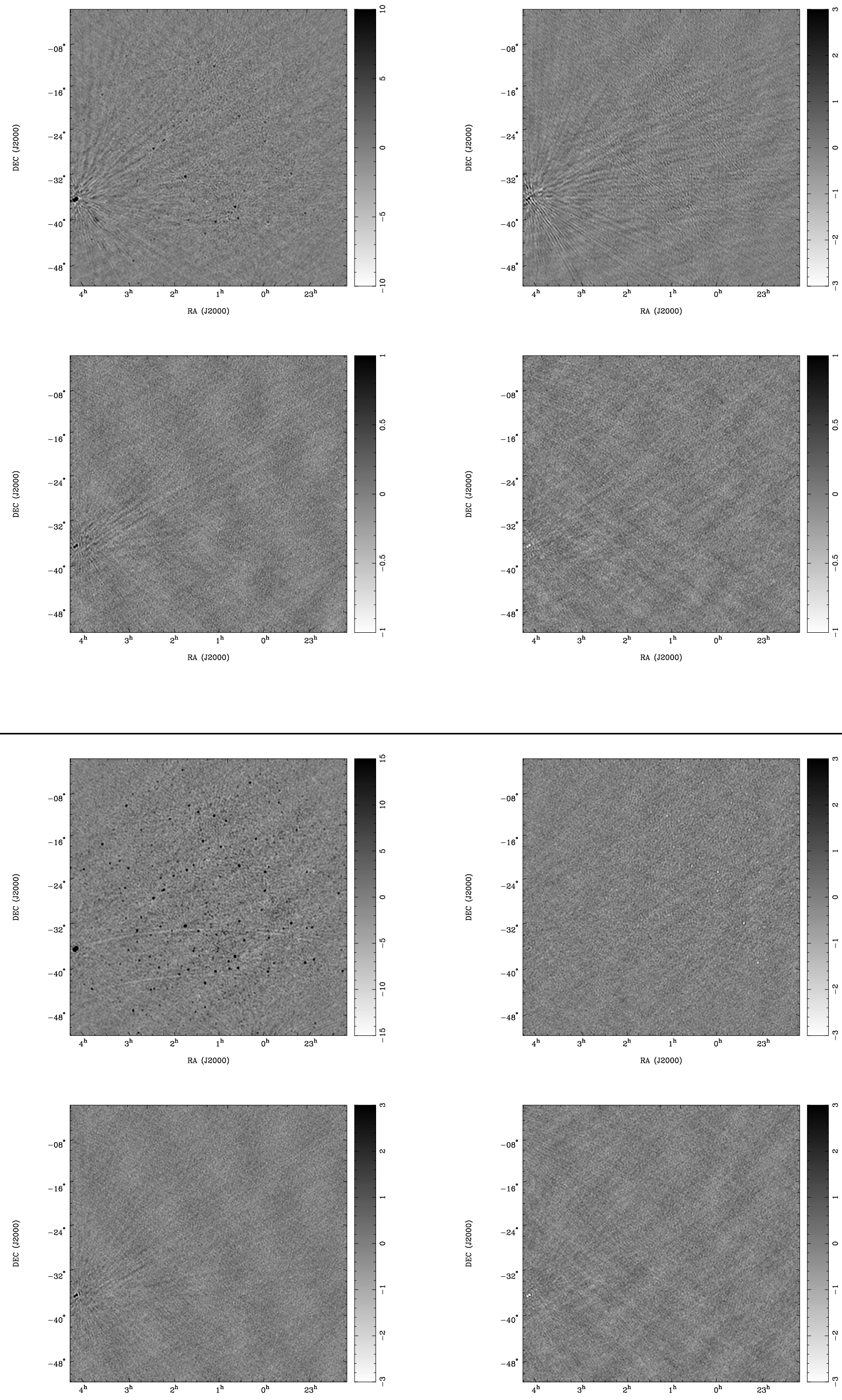

Figure 9.2: *Above:* Example of a Stokes I snapshot image (top left) with corresponding Stokes Q (top right), Stokes U (bottom left) and Stokes V (bottom right) images before absolute calibration. *Below:* The same organization as above, after absolute calibration. No primary beam correction was applied. The Stokes I image was deconvolved down to 5 Jy beam^{-1} whereas the other images were not deconvolved. Units are Jy beam^{-1}; note the change in scale between polarizations and calibration stages.

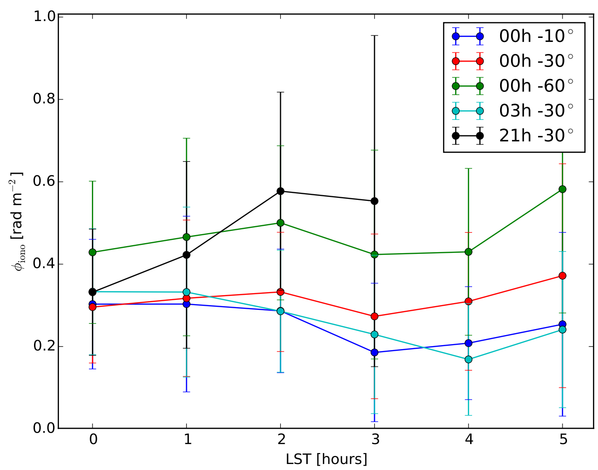

Figure 9.3: The values of ionospheric RM for different lines of sight the range of LSTs in this analysis, as calculated by IONFR (Sotomayor-Beltran et al., 2013). The 21h,0° line of sight goes beneath the horizon after LST=3h, and therefore has fewer data points.

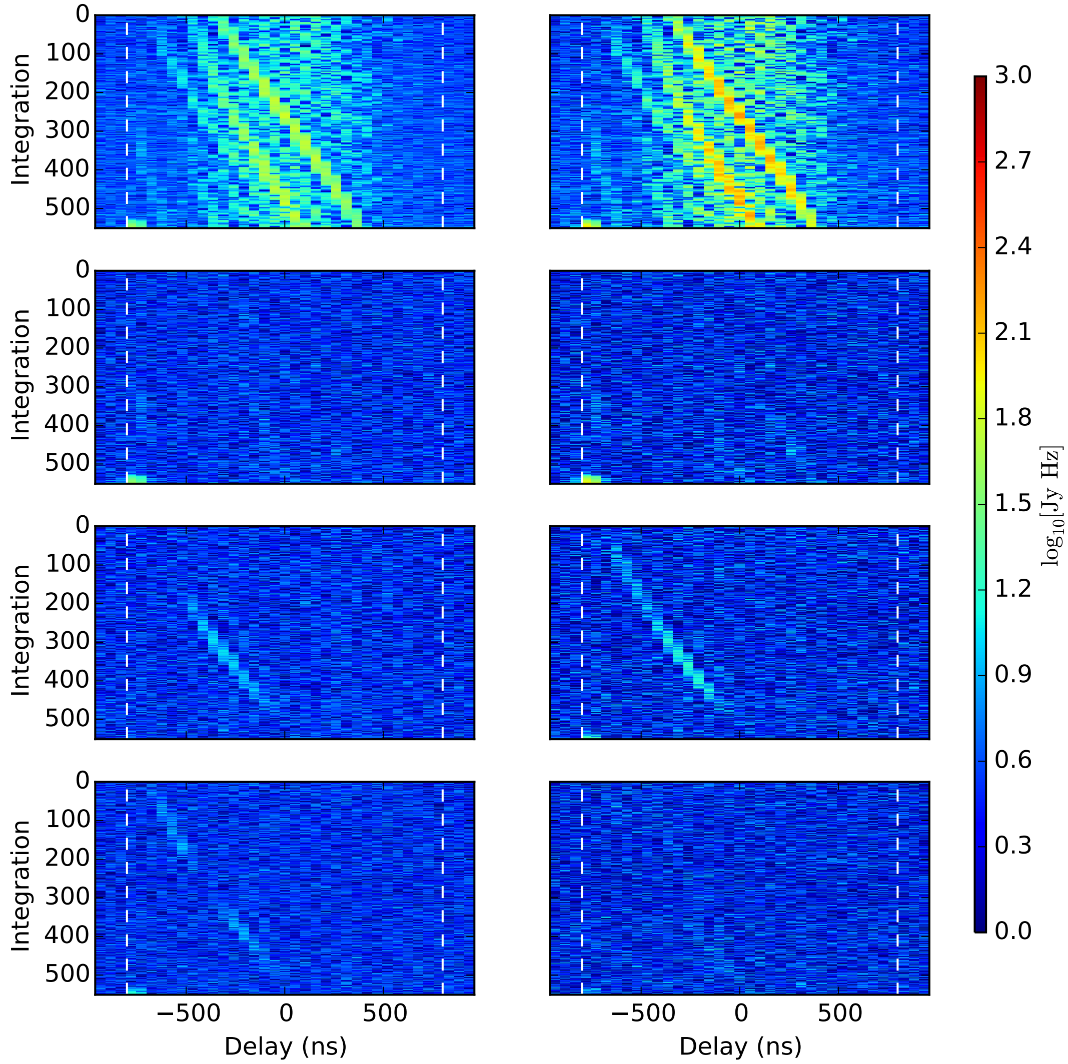

Figure 9.4: The absolute value of delay-transformed visibilities over the bandwidth (146–166 MHz) used to create the power spectra shown in this Chapter. The left and right columns show the visibilities before and after absolute calibration (and for Stokes U and V, the application of the τ_{xy} parameter), respectively, for baseline formed by antennae 6 and 14 ($\sim$ 250 m in length, approximately East-West). The flux scale in the left column as been boosted for a more fair comparison to the absolute-calibrated data. From top to bottom, the rows correspond to Stokes I, Q, U and V. The horizon limit is marked by white dashed lines.

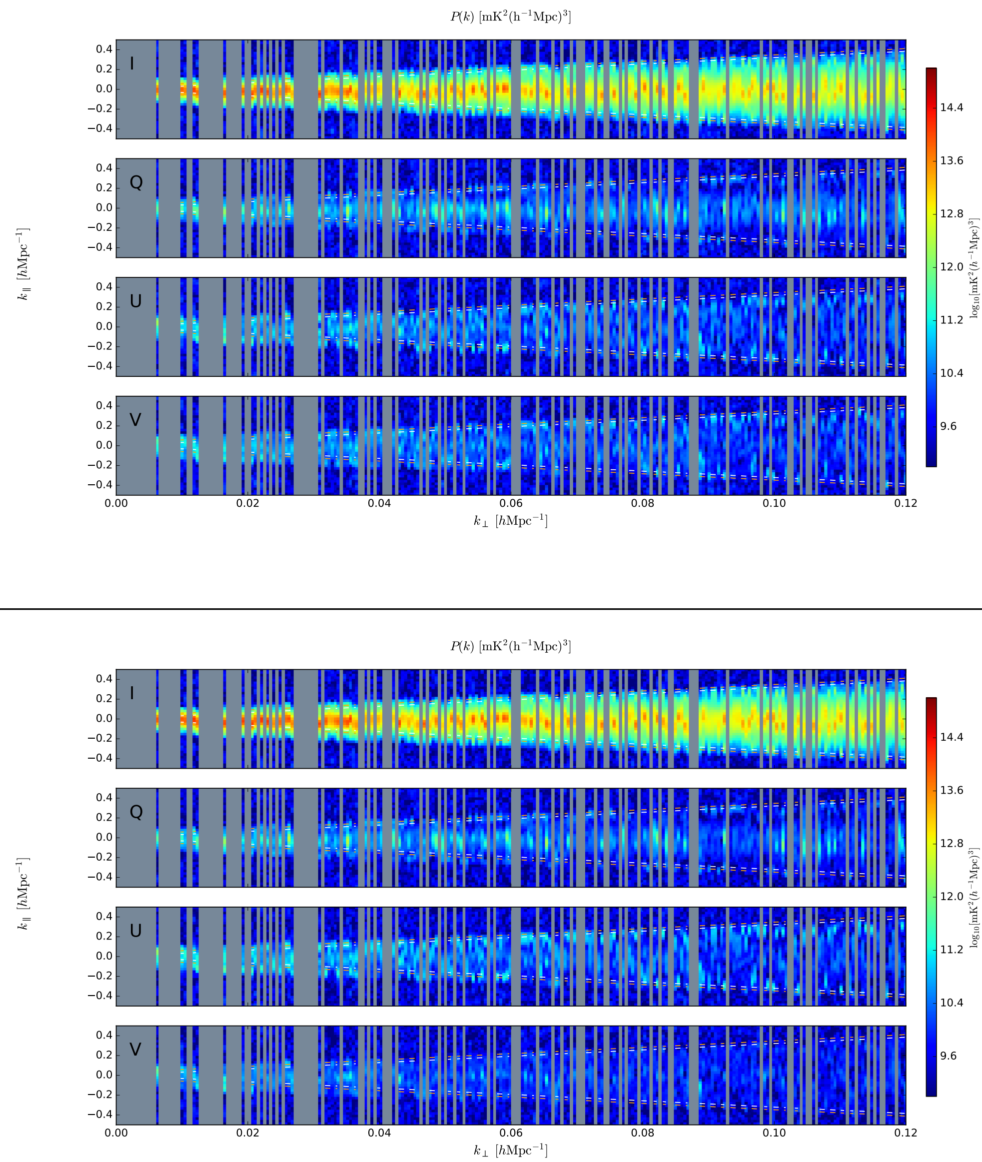

Figure 9.5: *Above:* Log-scaled 2D power spectra formed from (*top to bottom*): I, Q, U and V visibilities after before absolute calibration. Blank regions indicate the incomplete uv coverage for a given $k_\perp(u)$. The colorbar spans 10^9 to 10^{15} $\mathrm{mK}^2(h^{-1}\mathrm{Mpc})^3$. The flux scale has been boosted for a more fair comparison to the absolute-calibrated data. *Below:* The same organization as above, but after absolute calibration. Briefly, the structure in Stokes I is consistent with a point-source-dominated field with a weak diffuse component. The other Stokes parameters are consistent with calibration errors and systematics: Stokes Q shows gain errors on specific antennae, Stokes U gives an estimate of possible D-term leakage, and any structure in V shows unaccounted-for systematics, due to D-terms or mis-oriented antennae.

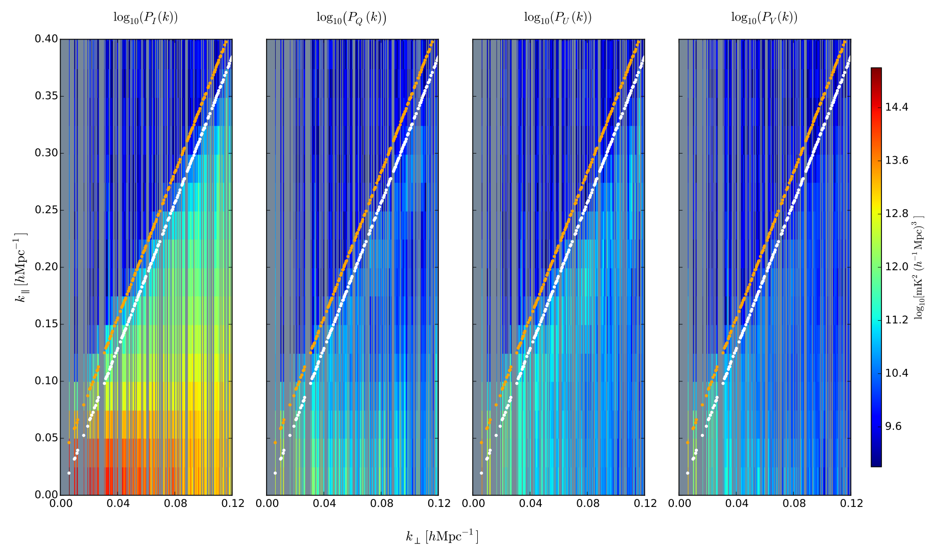

Figure 9.6: Log-scaled 2D power spectra formed from (*left to right*): I, Q, U and V absolute-calibrated visibilities. Blank regions indicate the incomplete *uv* coverage for a given $k_\perp(u)$. White and orange lines indicate the horizon and horizon plus a 50 ns boundary for super-horizon emission.

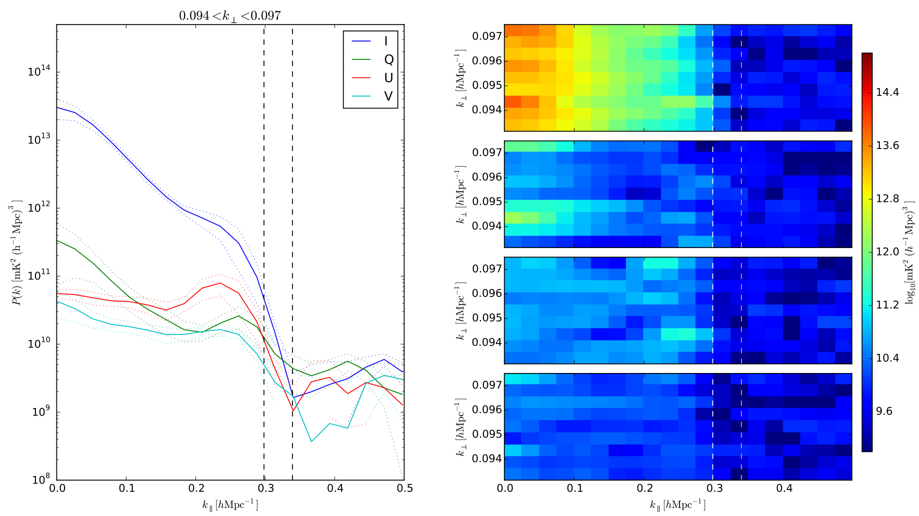

Figure 9.7: *Left*: The average power in $0.093 < k_\perp < 0.098\,h\mathrm{Mpc}^{-1}$ as a function of $k_\parallel$ for each polarization. In the horizon–super-horizon range that we see the sharp fall-off in power indicative of the edge of the EoR window. Outside of the wedge, Stokes I, Q and U are at noise level, while Stokes V is below noise level, most likely due to the τ_{xy} calibration scheme removing a degree of freedom from this Stokes parameter. *Right*: the region of k-space that was averaged over to create the lines in the left panel. From top to bottom, the panels correspond to Stokes I, Q U and V.

Chapter 10

A view of the EoR window from the HERA-19 commissioning array

As emphasized in Chapter 9, it is important to constrain intrinsic and leaked polarized signal for any EoR experiment. The objective of this Chapter was an exploration of eight nights of data from the Hydrogen Epoch of Reionization Array (HERA) 19-element commissioning array, coupled with simulations of the instrument, in order to forecast how much of a problem polarization would pose for this interferometer. This work also represents the first power spectral analysis from HERA. While not in the realm of an EoR-level integration, we were able to offer some initial expectations for this new instrument's performance in the Fourier domain.

This work is organized as follows: in Section 10.1 we review the theory behind polarization leakage into unpolarized signal and simulate the effect for a model of HERA. In Section 10.2 we describe the HERA data that we used, its calibration and reduction to power spectra. We present our results, and discuss the implications for HERA's EoR measurements, in Section 10.3, and conclude in Section **??**. We assume the cosmological parameters reported by Planck Collaboration et al. (2016) throughout.

10.1 Polarization Leakage Simulations

10.2 Observations & Reduction

In this work we used eight nights of observations from the HERA-19 commissioning array. HERA is a low-frequency interferometer composed of 14 m-diameter dishes arranged in a close-packed hexagonal array of 14.7 m spacing. The commissioning array consists of nineteen dishes (see Figure 10.1); HERA is being constructed in staged build-outs, and upon completion will consist of 350 dishes in a fractured hexagon configuration (see Dillon & Parsons, 2016; DeBoer et al., 2017). A feed cage containing two dipole feeds (recycled from the PAPER array, see Parsons et al. 2010), oriented in North-South and East-West directions, is suspended above each dish (Neben et al., 2016).

HERA only observes in drift-scan mode. The observations we used were eight nights, from Julian Date (JD) 2457548 to 2457555; LSTs 10.5 – 23 hr. Drift-scan visibilities were recorded every 10.7 seconds for 1024 evenly-spaced channels across the 100-200 MHz bandwidth. These data were divided into MIRIAD data sets roughly 10 minutes long. A night's observation lasted 12 hours in total (6pm to 6am South African Standard Time; SAST); of these we used the central 10 hours, to avoid thermal effects of the Sun.

To identify samples contaminated by radio frequency interference (RFI), a two-dimensional median filter in time and frequency was applied to the visibility data to smooth out high pixel-to-pixel variations, and remove significant outliers that were likely unphysical. The variance of the resulting data was computed, and points with a z-score greater than 6 (i.e., points where the value is more than 6σ away from the mean) were flagged as initial seeds for RFI extraction. A two-dimensional watershed algorithm was applied using these seeds as starting points, enlarging the regions of RFI-contamination to neighboring pixels with z-scores greater than 2, until all such pixels were flagged. Figure 10.2 shows the fractional RFI flag occupancy per time (displayed in LST) and frequency across the 8 days of observations. The majority of the band is relatively clear of RFI. Some clear features are: the FM radio band (below 120 MHz), ORBCOMM satellite communications (137 MHz),

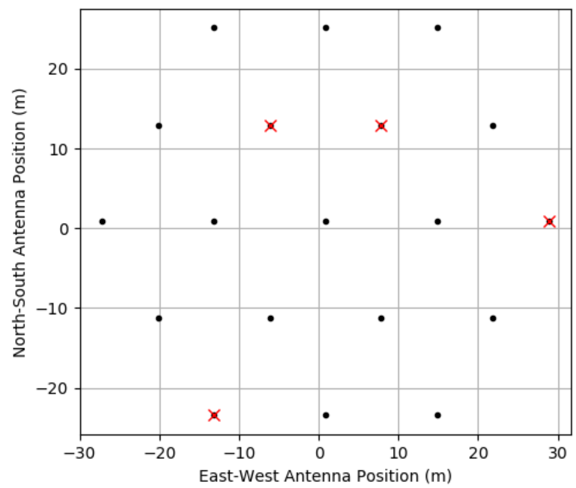

Figure 10.1: The centroid position of each dish in the HERA-19 array. A red "X" marks antennae that were malfunctioning during preprocessing and calibration, and were excluded from further analysis.

an ISS downlink (150 MHz) and VHF TV channels (above 170 MHz) [1]. The Galaxy, when transiting zenith at LST≈17.75, is so bright that it appears to degrade our ability to flag RFI.

10.2.1 Calibration

To perform calibration in CASA (McMullin et al., 2007), we converted between MIRIAD and UVFITS file formats using PYUVDATA (Hazelton et al., 2017). UVFITS files could be ingested by CASA.

Using LSTs in which the Galactic center (GC; α, δ = 17h 45m 40.04s,âĂŃ âĂŃ-29d 0m 28.12s) was transiting, we built a CLEAN model which modelled the GC as an unpolarized point source of strength 1 Jy and flat spectrum, which could be scaled appropriately later (see Equation 10.1). Clearly, this was an incomplete calibration model. However, as the objective of this work was to explore the response of the instrument in

[1]For an extended discussion of RFI as seen by HERA, see Chapter 6.

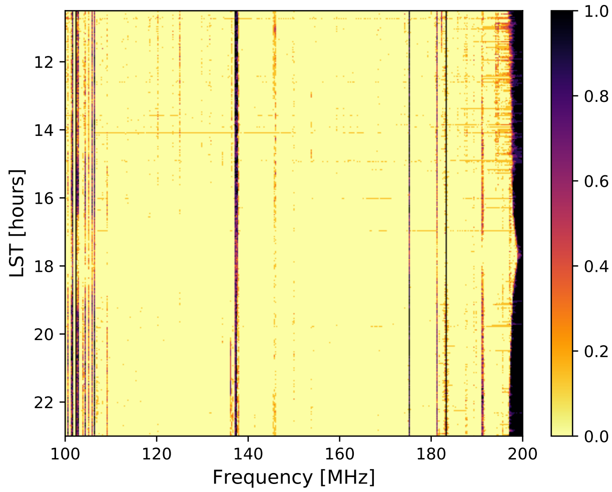

Figure 10.2: Fractional RFI flag occupancy per time and frequency over the eight days of observations.

power spectrum space: that is, not combining baselines of different lengths, most of the purpose of the calibration is correcting an initial large cable delay per antenna. Treating the GC as unpolarized is also adequate for this study. The large optical depth towards the GC (Oppermann et al., 2012) results in large amounts depolarization in the plane of the Galaxy (Wolleben et al., 2006). Moreover, we expect non-negligible amounts of beam depolarization from the instrument (Neben et al., 2016).

We used the `CASA` `gaincal` and `bandpass` functions to obtain frequency-dependent phase and amplitude solutions for each antenna and dipole arm. Four antennae had very deviant solutions, and their inclusion resulted in low-quality quality images. These were omitted from further analysis (and are marked with red "X"s in Figure 10.1). Before calibration, we manually flagged the edges of the band (below 110 MHz and above 190 MHz), where spectral behavior is dominated by the high and low pass filtering in the HERA signal chain (DeBoer et al., 2017).

Dirty images after calibration are shown in Figure 10.3. These are multi-frequency synthesis images, where we used all unflagged frequencies on either side of the band

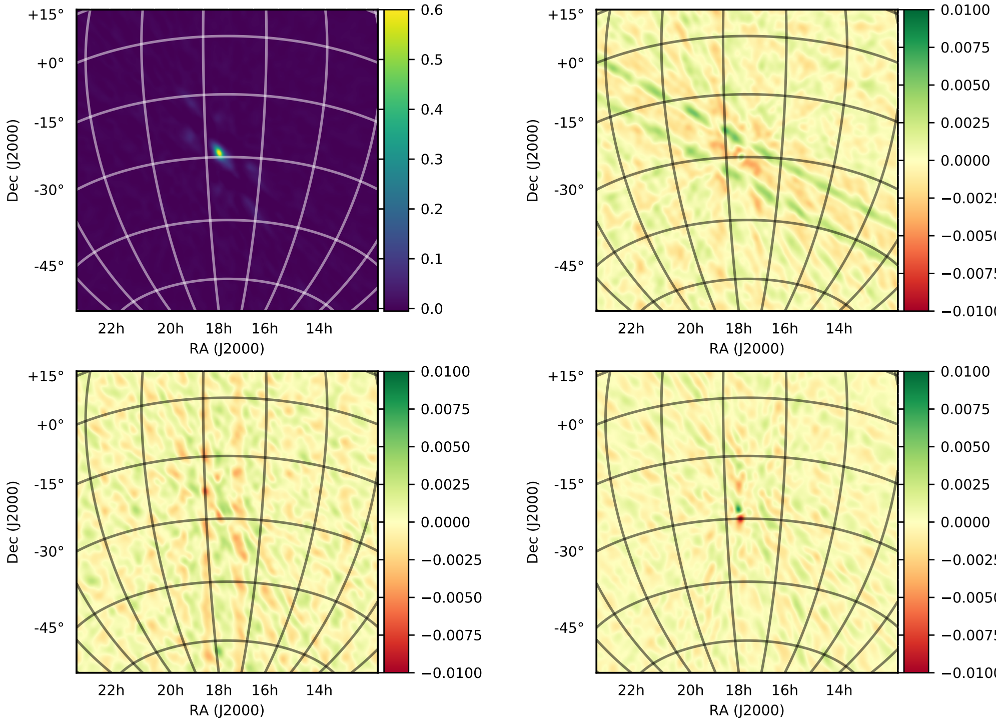

Figure 10.3: Multi-frequency synthesis images of the Galactic Center (our calibrator source) on JD 2457548 in Stokes I, Q, U and V (*top left, top right, lower left, lower right*). The colorbar is in units of Jy/Beam (relative to the 1 Jy source model; visibilities were later scaled according to Equation 10.1). A separate color scale is used for Stokes I for suitable dynamic range. An R.A., Dec. grid is shown, illustrating the wide-field nature of HERA observations.

edges; 115 MHz to 188 MHz. As expected for a compact array, the Stokes I images capture only the large-scale structure of the Galactic plane.

Example bandpass solutions from JD 2457548 are shown in Figure 10.4. Although some residual RFI remains obvious, the bandpass is smooth and should therefore not couple significant amounts foreground signal into the EoR window.

The complex gain solutions were subsequently applied to the MIRIAD files. Figure 10.5 shows the effect of calibration on visibilities three nominally redundantly-spaced baselines. Shown in that figure are the phases of three V_{nn} visibilities from 14.7 m base-

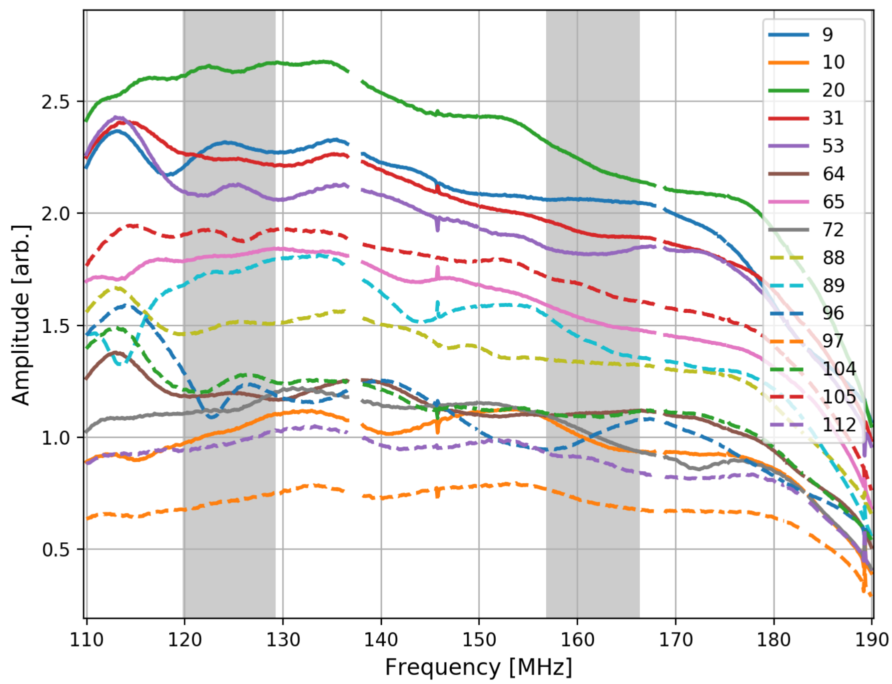

Figure 10.4: Bandpass solutions for the North-South dipole orientation obtained for the functioning antennae in the array on JD 2457548. Antennae are numbered according to their position in the final, 350-element array, leading to apparent out-of-order numbering for the commissioning array. Shaded regions indicate the sub-bands used for power spectrum analysis.

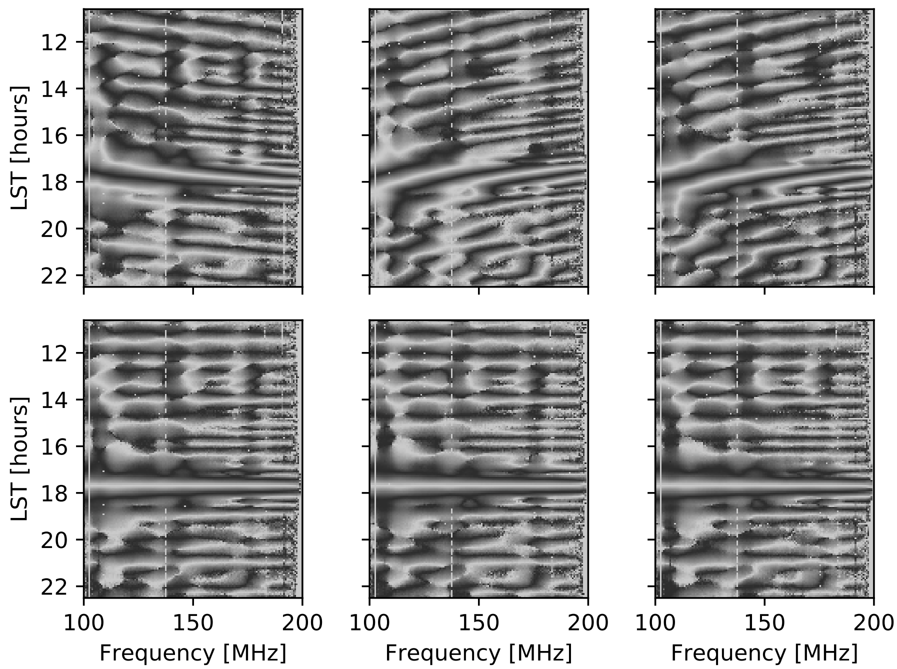

Figure 10.5: The effect of calibration on the phases of visibilities from three redundantly-spaced 14.7 m baselines; *nn* polarization. The color scale is cyclic; black is $\pm\pi/2$ and white is 0 and $\pm\pi$. *Above*: before calibration; *below*: after calibration. A simple sky model was sufficient to enforce redundancy for redundant baselines.

lines before and after calibration. There were no shared antennae between the visibilities shown. Our calibration was sufficient to enforce redundancy between these nominally-redundant baselines, which granted some verification of our methods.

We did not attempt to calibrate *D*-terms in this work as there were no polarized sources identified at low frequencies in the field surveyed, which are required for *D*-term calibration. This limited our interpretive power, which we discuss in Section 10.3.

We down-selected to two relatively RFI-free 10 MHz sub-bands; 120 to 130 MHz and 157 to 167 MHz, henceforth referred to the “low band" and the “high band". These thinner bands are representative of the range of frequencies one could use to claim an EoR detection, since the HI signal would be coeval over such a redshift range (Furlanetto et al.,

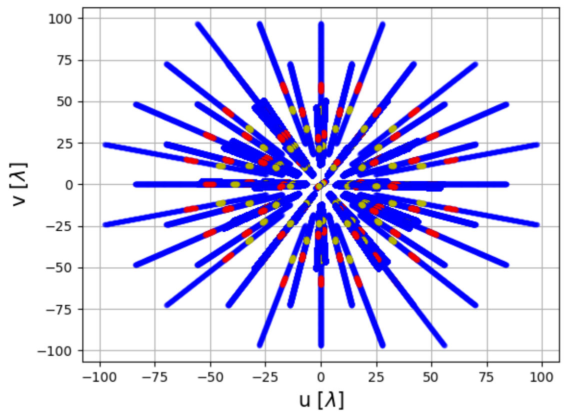

Figure 10.6: The instantaneous *uv*-coverage of the array. The *uv*-coverage of the full band, used for calibration and imaging, is shown in blue. The *uv*-coverage high and low bands are shown in red and yellow, respectively.

2006). As shown in Figure 10.2, they are both relatively clear of RFI. The instantaneous *uv*-coverage of the whole band is shown in blue in Figure 10.6, with the low and high bands shown in yellow and red, respectively.

Pseudo-Stokes visibilities were formed from the instrumental polarizations. These visibilities were then scaled to the appropriate amplitude using the power law

$$S_{\mathrm{SgrA}^*}(\nu) = 3709\,\mathrm{Jy} \times (\nu/408\,\mathrm{MHz})^{-2.5} \tag{10.1}$$

which is drawn from the Haslam map (Haslam et al., 1981, 1982; Remazeilles et al., 2015).

10.2.2 Forming power spectra

Power spectra were formed according to the method used in Pober et al. (2013), Kohn et al. (2016) and Chapter 9, which we briefly review here. All Fourier transforms were windowed using a Blackman-Harris window at the center of the sub-band, which minimized sidelobes. Parsons et al. (2012b) define the delay transform as the Fourier transform of a visibility for baseline ij and pseudo-Stokes parameter P along the frequency axis

$$\tilde{V}_{ij}^{P}(\tau,t) = \int \mathrm{d}\nu \tilde{V}_{ij}^{P}(\nu,t) e^{2\pi i\nu\tau} \tag{10.2}$$

The power at each delay-mode and baseline can be represented in terms of their respective Fourier components $k_{\parallel}$ and $k_{\perp}$ (Parsons et al., 2012b; Thyagarajan et al., 2015a):

$$P(k_{\parallel},k_{\perp}) = |\tilde{V}_{ij}^{P}(\tau,t)|^2 \frac{X^2 Y}{\Omega B}\left(\frac{c^2}{2k_B\nu^2}\right)^2,$$

$$k_{\parallel} = \frac{2\pi\nu_{21\mathrm{cm}} H_0 \sqrt{\Omega_m(1+z)^3+\Omega_k(1+z)^2+\Omega_\Lambda}}{c(1+z)^2}\tau,$$

$$k_{\perp} = \frac{2\pi}{D(z)\lambda} b \tag{10.3}$$

for: bandwidth B, angular area of the beam Ω, $\nu_{21\mathrm{cm}} \approx$1420 MHz, baseline length b, wavelength of observation λ, transverse comoving distance $D(z)$ and redshift-dependent scalars X and Y (Parsons et al., 2012a).

To form avoid a noise-bias when forming the $|\tilde{V}_{ij}^{P}(\tau,t)|^2$ term, we cross-multiplied consecutive integrations, rephasing the zenith angle of the latter to the former:

$$|\tilde{V}_{ij}^{P}(\tau,t)|^2 \approx |\tilde{V}_{ij}^{P}(\tau,t) \times \tilde{V}_{ij}^{P}(\tau,t+\Delta t) e^{i\theta_{ij,\mathrm{zen}}(\Delta t)}| \tag{10.4}$$

Where $\theta_{ij,\mathrm{zen}}(\Delta t)$ was the appropriate phasing for baseline ij and $\Delta t = 10.7$ seconds.

Power spectra were formed for each integration, for every baseline. Baselines of redundant lengths were then averaged together. Appealing to cosmological isotropy, baselines of the same length but different orientation should be sampling the same cosmological structure.

10.3 Results & Discussion

10.4 Conclusions

Chapter 11

Deep integrations on polarization with PAPER-128

Part III

Expanding the potential of EoR measurements

Chapter 12

Time-Averaged Visibilities

Chapter 13

Higher-order correlation functions between kSZ and 21cm observations

Chapter 14

Deep Learning for 21cm Observations

Chapter 15

Conclusions

Appendices

Appendix A

Software

Software engineering and maintenance of existing codebases has been, generally speaking, historically undervalued and unappreciated by the astronomy community (Muna et al., 2016). In this Appendix I would like to provide a brief description of the major software packages used in this work – without which, the work would not exist.

A.1 Astronomical Interferometry in Python (`aipy`)

The `aipy` software package (Parsons, 2016) was developed by a team based largely at the University of California, Berkeley and led by Aaron Parsons. Developed under NSF funding for the PAPER experiment, it provides a Python API to interact with interferometric visibilities stored in the MIRIAD file format (Sault et al., 2011). It is able to efficiently query large MIRIAD files due the APIs closeness to the underlying C code. It also contains calibration, deconvolution, imaging and phasing code in Python, and interfaces with `HEALPix` (see Section A.5, below) as well as other astronomical Python packages.

`aipy` is maintained by the HERA software team, and can be found at: `https://github.com/HERA-Team/aipy`.

A.2 Astronomy in Python (`astropy`)

`astropy` is an open-source and community-developed core Python package for Astronomy, containing a host of extremely useful utility functions and objects (Astropy Collaboration et al., 2013).

A.3 Common Astronomy Software Applications (`CASA`)

`CASA` is under active development, with the primary goal of supporting the data post-processing needs of the next generation of radio telescopes. It is developed by an international consortium of scientists based at the National Radio Astronomical Observatory (NRAO), the European Southern Observatory (ESO), the National Astronomical Observatory of Japan (NAOJ), the CSIRO Australia Telescope National Facility (CSIRO/ATNF), and the Netherlands Institute for Radio Astronomy (ASTRON), under the guidance of NRAO (McMullin et al., 2007).

A.4 Deep Learning packages

Experimentation with deep learning analyses of 21 cm simulated observations took place in Keras (Chollet et al., 2015), PyTorch (Paszke et al., 2017) and Tensorflow (Abadi et al., 2016).

A.5 Hierarchical Equal Area isoLatitude Pixelization of the sphere (`HEALPix`)

The `HEALPix` software, and its Python wrapper `healpy`, provide a pixelization which subdivides a spherical surface into pixels which each cover the same surface area as every other pixel. Pixel centers occur on a discrete number of rings of constant latitude. This scheme makes natively spherical measurements, such as angular power spectra and wide-field images, simple and efficient to interact with (Górski et al., 2005).

A.6 `pyuvdata`

`pyuvdata` provides a Python interface to interferometric data. It can read and write MIRIAD and UVFITS file formats, as well as read `CASA` measurement sets and `FHD` (Sullivan et al., 2012b) visibility save files (Hazelton et al., 2017).

`pyuvdata` is maintained by the HERA software team, and can be found at: `https://github.com/HERA-Team/pyuvdata`.

A.7 The Scientific Python Ecosystem (`scipy`)

Many of the above tools require at least one of the many packages under the `scipy` ecosystem. It is truly foundational to almost any scientific analysis that takes place in Python (Jones et al., 2001).

Bibliography

Abadi, M. et al. 2016, ArXiv e-prints

Afraimovich, E. L., Astafyeva, E. I., Oinats, A. V., Yasukevich, Y. V., & Zhivetiev, I. V. 2008, Annales Geophysicae, 26, 335

Ali, Z. S. et al. 2015, ArXiv e-prints

Appleton, E. V. 1946, Nature, 157, 691

Asad, K. M. B., Koopmans, L. V. E., Jelić, V., de Bruyn, A. G., Pandey, V. N., & Gehlot, B. K. 2017, ArXiv e-prints

Asad, K. M. B. et al. 2016, MNRAS, 462, 4482

—. 2015, MNRAS, 451, 3709

Astropy Collaboration et al. 2013, A& A, 558, A33

Backer, D. C. et al. 2010, HERA âĂŞ Hydrogen Epoch of Reionization Arrays, Submitted for consideration by the Astro2010 Decadal Survey Program Panel

Bernardi, G. et al. 2013, ApJ, 771, 105

Brunner, F. K. & Welsch, W. M. 1993, GPS World, 4, 42

Carilli, C. L. & Rawlings, S. 2004, NewAR, 48, 979

Carozzi, T. D. & Woan, G. 2009, MNRAS, 395

Chollet, F. et al. 2015, Keras, `https://github.com/fchollet/keras`

Civil Aviation Authority. 2016, http://www.caa.co.za/Pages/Search-results.aspx?k=frequency#k=113.3%20MHz, website

Condon, J. J., Cotton, W. D., Greisen, E. W., Yin, Q. F., Perley, R. A., Taylor, G. B., & Broderick, J. J. 1998, AJ, 115, 1693

Cornwell, T. 2016

Cotton, W. & Condon, J. 2002, in Proceedings of the URSI General Assembly

DeBoer, D. R. et al. 2017, PASP, 129, 045001

Dewdney, P. E., Hall, P. J., Schilizzi, R. T., & Lazio, T. J. L. 2009, Proceedings of the IEEE, 97, 1482

Dillon, J. S. et al. 2014, Phys. Rev. D, 89, 023002

—. 2015, Phys. Rev. D, 91, 123011

Dillon, J. S. & Parsons, A. R. 2016, ApJ, 826, 181

Erdogan, E. et al. 2016, in EGU General Assembly Conference Abstracts, Vol. 18, EGU General Assembly Conference Abstracts, 12685

Erickson, W. C., Perley, R. A., Flatters, C., & Kassim, N. E. 2001, A&A, 366, 1071

Ewall-Wice, A. et al. 2016, ApJ, 831, 196

Finlay, C. C. et al. 2010, Geophysical Journal International, 183, 1216

Furlanetto, S. R., Oh, S. P., & Briggs, F. H. 2006, Physics Review, 433, 181

Geil, P. M., Gaensler, B. M., & Wyithe, J. S. B. 2011, MNRAS, 418, 516

Górski, K. M., Hivon, E., Banday, A. J., Wandelt, B. D., Hansen, F. K., Reinecke, M., & Bartelmann, M. 2005, ApJ, 622, 759

Hamaker, J. P., Bregman, J. D., & Sault, R. J. 1996, A&AS, 117, 137

Haslam, C. G. T., Klein, U., Salter, C. J., Stoffel, H., Wilson, W. E., Cleary, M. N., Cooke, D. J., & Thomasson, P. 1981, A& A, 100, 209

Haslam, C. G. T., Salter, C. J., Stoffel, H., & Wilson, W. E. 1982, A& ASS, 47, 1

Hazelton, B., Beardsley, A., Pober, J., Jacobs, D., Ali, Z., & Lanman, A. 2017, HERA-Team/pyuvdata: Version 1.1

Hazelton, B. J., Morales, M. F., & Sullivan, I. S. 2013, ApJ, 770, 156

Hurley-Walker, N. et al. 2017, MNRAS, 464, 1146

Iijima, B. et al. 1999, Journal of Atmospheric and Solar-Terrestrial Physics, 61, 1205

Intema, H., Van der Tol, S., Cotton, W., Cohen, A., Van Bemmel, I., & Röttgering, H. 2009, Astronomy & Astrophysics, 501, 1185

Jacobs, D. C. et al. 2016, ApJ, 825, 114

—. 2013, ApJ, 776, 108

—. 2015, ApJ, 801, 51

Jelić, V. et al. 2014, A&A, 568, A101

—. 2015, A&A, 583, A137

Jones, E., Oliphant, T., Peterson, P., et al. 2001, SciPy: Open source scientific tools for Python, [Online; accessed <today>]

Klobuchar, J. A. 1983, Ionospheric Effects on Earth-Space Propagation

Kohn, S. A. et al. 2016, ApJ, 823, 88

Komjathy, A., Sparks, L., Wilson, B. D., & Mannucci, A. J. 2005, Radio Science, 40

Lanyi, G. E. & Roth, T. 1988, Radio Science, 23, 483

Lenc, E. et al. 2017, PA&A, 34, e040

—. 2016, ApJ, 830, 38

Loi, S. T. et al. 2015, Geophys. Res. Lett., 42, 3707

MacDoran, P. & Spitzmesser, D. 1989, Method and apparatus for deriving pseudo range from earth-orbiting satellites, uS Patent 4,797,677

Mannucci, A., Wilson, B., Yuan, D., Ho, C., Lindqwister, U., & Runge, T. 1998, Radio science, 33, 565

McMullin, J. P., Waters, B., Schiebel, D., Young, W., & Golap, K. 2007, in Astronomical Data Analysis Software and Systems XVI, ed. R. A. Shaw, F. Hill, & D. J. Bell, 376, ASP, San Francisco, CA, 127

Mevius, M. et al. 2016, Radio Science, 51, 927

Mohan, N. & Rafferty, D. 2015, PyBDSM: Python Blob Detection and Source Measurement, Astrophysics Source Code Library, record 1502.007

Moore, D. F. 2014, PhD thesis, University of Pennsylvania

Moore, D. F. et al. 2017, ApJ, 836, 154

Moore, D. F., Aguirre, J. E., Parsons, A. R., Jacobs, D. C., & Pober, J. C. 2013, ApJ, 769, 154

Morales, M. F., Hazelton, B., Sullivan, I., & Beardsley, A. 2012, ApJ, 752, 137

Muna, D. et al. 2016, ArXiv e-prints

Neben, A. R. et al. 2016, ApJ, 826, 199

NRC, N. R. C. 2010, New Worlds, New Horizons in Astronomy and Astrophysics (Washington, DC: The National Academies Press)

Nunhokee, C. D. et al. 2017, ApJ, 848, 47

Offringa, A. R., van de Gronde, J. J., & Roerdink, J. B. T. M. 2012, A&A, 539, A95

Oppermann, N. et al. 2012, A& A, 542, A93

Parsons, A. 2016, AIPY: Astronomical Interferometry in PYthon, Astrophysics Source Code Library

Parsons, A. et al. 2008, PASA, 120, 1207

Parsons, A., Pober, J., McQuinn, M., Jacobs, D., & Aguirre, J. 2012a, ApJ, 753, 81

Parsons, A. R. & Backer, D. C. 2009, AJ, 138, 219

Parsons, A. R. et al. 2010, AJ, 139, 1468

—. 2014, ApJ, 788, 106

Parsons, A. R., Pober, J. C., Aguirre, J. E., Carilli, C. L., Jacobs, D. C., & Moore, D. F. 2012b, ApJ, 756, 165

Paszke, A. et al. 2017

Patil, A. H. et al. 2017, ApJ, 838, 65

Pen, U.-L., Chang, T.-C., Hirata, C. M., Peterson, J. B., Roy, J., Gupta, Y., Odegova, J., & Sigurdson, K. 2009, MNRAS, 399, 181

Planck Collaboration et al. 2016, A& A, 594, A13

Pober, J. 2015, Updated 21cm Experiment Sensitivities, Tech. Rep. 4, Brown University

Pober, J. C. et al. 2015, ApJ, 809, 62

—. 2013, ApJL, 768, L36

—. 2012, AJ, 143, 53

Price, D. C. 2016, ArXiv e-prints

Remazeilles, M., Dickinson, C., Banday, A. J., Bigot-Sazy, M.-A., & Ghosh, T. 2015, MNRAS, 451, 4311

Royden, H., Miller, R., & Buennagel, L. 1984, Radio science, 19, 798

Sault, R. J., Hamaker, J. P., & Bregman, J. D. 1996, A&AS, 117, 149

Sault, R. J., Teuben, P., & Wright, M. C. H. 2011, MIRIAD: Multi-channel Image Reconstruction, Image Analysis, and Display, Astrophysics Source Code Library

Schilizzi, R. et al. 2007, SKA Memorandum, 100

SKA Panel. 2012, Expert Panel on Radio Quiet Zone and RFI Regulation Report, Tech. rep., Square Kilometer Array, https://www.skatelescope.org/wp-content/uploads/2012/06/79_Report_of_The_Expert_Panel_on_Radio_Quiet_Zone_and_RFI_Regulation.pdf

Smirnov, O. M. 2011, A&A, 527, A106

Sotomayor-Beltran, C. et al. 2013, A&A, 552, A58

South African Civil Aviation Authority. 2008, FLIGHT CALIBRATION DATES OF VOR's IN THE REPUBLIC OF SOUTH AFRICA, Tech. Rep. 25.6, Aeronautical Information Circular, http://209.203.9.244/resource%20center/AIC'S/25.6.pdf

Staatskoerant. 2008, South African Table of Frequency Allocations, Tech. Rep. 31264, ICASA, http://thornton.co.za/resources/31264_890_complete-1.pdf

Stefan, I. I. et al. 2013, MNRAS, 432, 1285

Sullivan, I. S. et al. 2012a, ApJ, 759, 17

—. 2012b, ApJ, 759, 17

Tariku, Y. A. 2015, Earth, Planets, and Space, 67, 35

Thompson, A. R., Moran, J. M., & Swenson, Jr., G. W. 2017, Interferometry and Synthesis in Radio Astronomy, 3rd Edition

Thyagarajan, N. et al. 2015a, ApJ, 804, 14

—. 2015b, ApJ, 807, L28

Titheridge, J. E. 1972, P& SS, 20, 353

Trott, C. M. et al. 2016, ApJ, 818, 139

van Haarlem, M. P. et al. 2013, A&A, 556, A2

Vedantham, H. K. & Koopmans, L. V. E. 2015, MNRAS, 453, 925

—. 2016, MNRAS, 458, 3099

Wolleben, M., Landecker, T. L., Reich, W., & Wielebinski, R. 2006, A& A, 448, 411

World Aero Data. 2016, http://worldaerodata.com/wad.cgi?nav=VICTORIA+WEST&nav_id=VWV&na website

Yatawatta, S. et al. 2013, A&A, 550, A136

Zolesi, B. & Cander, L. R. 2014, Ionospheric prediction and forecasting (Springer)